

Control and Stability of Modular DC Swarm Microgrids

Hannes Kirchhoff¹ and Kai Strunz²

Abstract—Direct current (dc) microgrids have not yet achieved the promise of true plug-and-play characteristics due to stability issues stemming from power converters. Swarm microgrids, a type of dc microgrids, are aimed at delivering a modular and easy-to-expand infrastructure. In this article, an application-specific control strategy is developed to ensure stable and expandable swarm microgrids. This control strategy makes use of the widely available distributed storage in swarm microgrids and includes active damping techniques at power-drawing units. Utilizing a cascaded state-space system model, experimental validation with dual-active-bridge converters, and eigenvalue robustness analysis, this article demonstrates a high margin of stability for expandable swarm microgrids. The analysis includes variation of the microgrid size and line parameters, among others. The results show that swarm microgrids are stable for up to at least 1000 participating swarm units. As part of the robustness analysis of swarm microgrid stability, specific definitions are provided for the allowed behavior of the power converters used in a swarm microgrid. The developed methodology allows assessing and designing for swarm microgrid stability even without knowledge of the internal structures of the power converters. As such, this article provides a practical framework to support the scaling up of swarm microgrid deployment.

Index Terms—Control, direct current (dc), energy access, low voltage, microgrid, stability, swarm electrification.

Acronyms: NOMENCLATURE

CC	Current control.
CPL	Constant power load.
LPF	Low-pass filter.
LTI	Linear time-invariant.
SBB	Swarm building block.
SHS	Solar home system.
VC	Voltage control.

Subscripts and Indices:

0	Zero current.
1	First order.

Manuscript received 20 November 2021; revised 6 February 2022; accepted 25 March 2022. Date of publication 18 April 2022; date of current version 3 October 2022. This work was supported by the Hans-Böckler Foundation through a Ph.D. scholarship, which is co-funded by the Federal Ministry of Education and Research, Germany. Recommended for publication by Associate Editor Mahesh S. Illindala. (Corresponding author: Hannes Kirchhoff.)

Hannes Kirchhoff is with the Chair of Sustainable Electric Networks and Sources of Energy (SENSE), Department of Energy and Automation Technology, Technische Universität Berlin, 10587 Berlin, Germany, also with ME SOLshare Ltd., Dhaka 1229, Bangladesh, and also with ME SOLshare International Pte. Ltd., Singapore 068808 (e-mail: microenergy.kirchhoff@gmail.com).

Kai Strunz is with the Chair of Sustainable Electric Networks and Sources of Energy (SENSE), Department of Energy and Automation Technology, Technische Universität Berlin, 10587 Berlin, Germany (e-mail: kai.strunz@tu-berlin.de).

Color versions of one or more figures in this article are available at <https://doi.org/10.1109/JESTPE.2022.3168545>.

Digital Object Identifier 10.1109/JESTPE.2022.3168545

2	Second order.
c	Cable.
C	Capacitance.
ch	Charging.
diag	Diagonal elements.
dr	Droop.
g	Matrix index.
h	Matrix index.
in	Input.
j	Node index.
k	Cable index.
lab	Laboratory.
link	Link.
LPF	Low-pass filter.
n	Node, nodal.
ns	Number of swarm units operating in supplying mode.
o	Output.
pos	Positive.
re	Real part.
ref	Reference value.
s	Supplying.
sim	Simulation.
SMG	Swarm microgrid.
var	Variations.
Y	Input admittance.
z	Coupling output.
Z	Output impedance.

Variables and Operators:

A	System matrix.
A	Cross-sectional area.
B	Input matrix.
C	Output matrix.
C	Capacitance.
D	Direct feedthrough matrix.
f	Frequency.
g	Matrix index.
h	Matrix index.
i, I	Current.
j	Node index.
k	Cable index.
K	Gain.
\mathbb{K}	Parameter set.
l	Length.
L	Inductance.
m	Number of cables.
M	Incidence matrix.
n	Number of swarm units.
N	Total number.
P	Power.

r, R	Resistance.
s	Complex frequency.
\mathbf{s}	Coupling input vector.
\mathbf{S}	Coupling input matrix.
t	Time.
T	Time constant.
$T(s)$	Transfer function.
\mathbf{u}	Vector of control signals.
v, V	Voltage.
\mathbf{x}	State vector.
\tilde{x}	Small-signal perturbation of x .
\mathbf{y}	Output vector.
Y	Admittance.
\mathbf{z}	Coupling output vector.
Z	Impedance.
β	Qualitative robustness metric.
Δ	Difference operator.
ζ	Damping factor.
κ	Algebraic coupling.
σ	Conductivity.
Σ	System definition.

Notation: Vectors and matrices are written in bold type.

I. INTRODUCTION

GLOBALLY, 840 million people still lack access to electricity [1]. Swarm electrification is intended to address this undesirable situation by enabling the efficient usage of existing resources through the sharing of electricity within a neighborhood [2]. Swarm electrification facilitates the step-wise enhancement of energy access infrastructure using specially designed direct current (dc) microgrids, referred to as swarm microgrids [3]. A swarm microgrid facilitates peer-to-peer energy exchange between so-called swarm units. These swarm units are located at homes or businesses that already have existing standalone energy systems [4]. Important standalone energy systems are solar home systems (SHSs), of which six million units have been installed in Bangladesh alone [5]. Many of these SHSs have now been interconnected into swarm microgrids: The United Nations and other organizations have supported the rollout of over 100 swarm microgrids across Bangladesh [6], [7].

This article investigates the stability of swarm microgrids with up to 1000 units as an important hallmark of swarm electrification. Swarm microgrids are dc microgrids, and therefore, the literature on the stability of dc microgrids is relevant [8], [9], in particular with regards to: 1) microgrid control schemes; 2) stability assessment methods; and 3) converter modeling approaches.

In regard to dc microgrid control schemes, the literature differentiates between centralized control schemes [10], [11] and decentralized control schemes [12], [13]. Decentralized control schemes are the preferred choice for swarm microgrids, because swarm microgrids need to be deployable at hard-to-reach sites. Among the literature on decentralized control schemes, recent research has evaluated microgrid systems with constant power loads (CPLs) and droop-controlled sources, and the findings indicate that static droop control may lead to system instability [9], [14]–[17]. To provide stability, advanced droop

control methods can be used, many of which rely on the availability of energy storage in the microgrid [18]–[24]. In principle, these methods can also be applied to swarm microgrids because of the distributed storage capacity of SHSs [25], [26]. Research on the decentralized control of distributed storage units in dc microgrids has focused on the behavior of these units when supplying power [13], [20]. However, the decentralized control of distributed storage units when drawing power was not addressed to the extent needed for practical application.

In regard to stability assessment methods for dc microgrids, two main approaches are described in the literature: large-signal stability analysis and small-signal stability analysis. A large-signal stability analysis accounts for large disturbances but is usually only used to analyze single-bus microgrids [27], [28]. In a small-signal stability analysis, a linear model is constructed around a steady-state operating point [8], [12], [29]. The advantage of the small-signal stability analysis is the ability to easily adapt the model to assess different topological configurations of microgrids [25], [30], [31]. However, to date, most studies have been limited in the number of participating units assessed. The number of units is lower than five in [26], [30], and [31] and lower than ten in [9], [18], and [25].

For the modeling of power electronic converters in dc microgrids, two main approaches are discussed in the literature. On the one hand, the so-called white-box modeling approach is widely used. This means that a certain internal converter structure is assumed, and the converter behavior is modeled accordingly [21], [32], [33]. On the other hand, the so-called black-box modeling approach is based on measurements and, thus, real-world behavior [34]–[36]. The black-box modeling approach is an attractive option for the case of swarm microgrids, because the collective behavior of converters and distributed storage units can be reflected. A black-box modeling has been used to design and assess dc microgrids of different scales and with different types of converter topologies [37]–[39]. However, the existing literature lacks measurement-derived models of converters connected to batteries.

A systematic analysis that addresses these highlighted shortcomings of the literature is not yet available. Therefore, this article adds to the existing research with the following key contributions.

- 1) It develops a control strategy specific to the needs of swarm microgrids that ensures stability and makes use of the available distributed storage.
- 2) It demonstrates the stability for the expansion of a swarm microgrid up to 1000 swarm units.
- 3) It provides practical definitions of allowed and no-go areas for the black-box behavior of battery-connected converters to ensure a stable microgrid.

The rest of this article is structured as follows. The architecture and attributes of swarm microgrids are discussed in Section II. Section III describes the development of the proposed control strategy. The swarm microgrid model is derived in Section IV. An experimental validation is presented in Section V. A comprehensive stability analysis of swarm microgrids is performed in Section VI. The conclusions are drawn in Section VII.

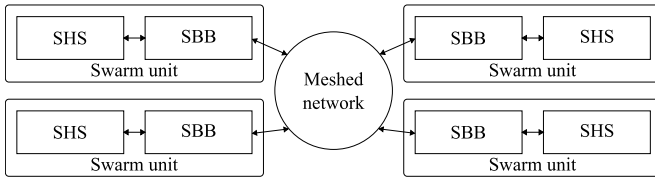


Fig. 1. Conceptual layout of a swarm microgrid consisting of so-called swarm units, each encompassing a solar home system (SHS) and a swarm building block (SBB).

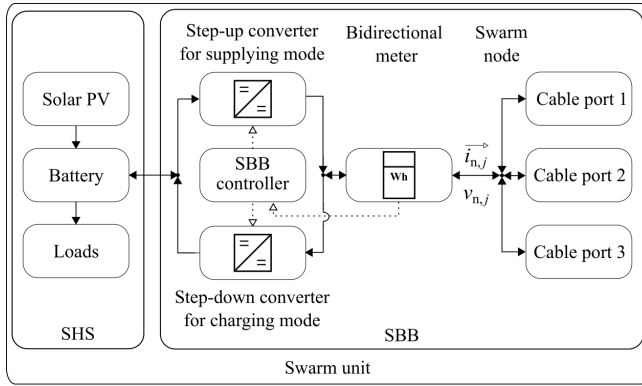


Fig. 2. Architecture of a swarm unit, including a solar home system (SHS) and a swarm building block (SBB); the node voltage $v_{n,j}$ and the nodal current $i_{n,j}$ are indicated.

II. ARCHITECTURE

The objectives of this section are twofold. First, the architecture of swarm microgrids is elaborated. Second, architectural attributes relevant for Sections III, IV, and VI are derived.

A. Architecture of Swarm Microgrids

The overall layout of a swarm microgrid as studied in this article is shown in Fig. 1 and described as follows. A swarm microgrid uses a meshed network to interconnect swarm units. A swarm unit consists of an SHS and a so-called swarm building block (SBB). The SBB enables bidirectional power flow between the SHS and other swarm units of the microgrid. Furthermore, an SBB provides the ability to form meshed network topologies in a modular manner. This modularity allows for continuous and organic growth; the swarm microgrid can be expanded at any time and should be able to cater for up to 1000 participants. A real-world example of swarm microgrid components in operation is provided in Appendix A. More details on the internal architecture of a swarm unit are provided in Fig. 2 and described as follows.

The SHS consists of solar photovoltaics (PVs), a battery, and loads. To enable bidirectional power flow between the SHS and other swarm units of the swarm microgrid, the SBB interfaces with the battery of the SHS and can operate in two distinct modes. The first mode is the supplying mode—the battery is discharged to supply the other swarm units of the microgrid. The second mode is the charging mode—energy is drawn from the other swarm units of the microgrid to charge the battery. These modes are realized using the following components, as shown in Fig. 2. A step-up converter is used for the supplying mode, and a step-down converter is used for the charging mode. Only one of the two modes can be selected at any given time.

To allow for adequate monitoring and billing, a bidirectional meter is required. The abovementioned components are

connected to the SBB controller, which enables the implementation of advanced control schemes. To provide the ability to form meshed network configurations, an SBB has cable ports, which allow for interconnection with other swarm units and can be used to realize zonal protection [40], [41]. These cable ports are joined at the swarm node. The node voltage between the positive and negative rails at swarm node j is denoted by $v_{n,j}$. The nodal current that is injected at node j is denoted by $i_{n,j}$. The nodal current $i_{n,j}$ takes negative values when the swarm unit is operating in the charging mode.

B. Attributes Relevant to Stability and Control

Based on the architecture presented earlier, swarm microgrids have certain characteristic attributes. Some of them are relevant to stability analysis. These attributes are directly related to the subsequent sections on the control strategy, system modeling, and stability analysis, as follows.

First, swarm microgrids are characterized by *ad hoc* deployment and ease of expansion even during operation. This attribute is particularly important in Section III when defining the control strategy, which must cater to this capability of *ad hoc* deployment.

Second, to reach a large number of users consistent with swarm electrification, a swarm microgrid is expected to support up to 1000 swarm units. This requirement is important for the overall modeling of the swarm microgrid, as discussed in Section IV, and for the stability analysis undertaken in Section VI.

Third, there are two distinct modes in which a swarm unit can operate: the supplying mode and the charging mode. The distinction between these two modes is a key input to the design of the cascaded system model, as discussed in Section IV-A. As shown in Fig. 2, the supplying mode is characterized by the usage of only the step-up converter. The charging mode is characterized by the usage of only the step-down converter.

Fourth, from a network stability point of view, only the side of the converter that is connected to the swarm node, as indicated in Fig. 2, is of interest. This means that in the supplying mode, only the behavior of the output side of the step-up converter is of interest; in the charging mode, only the behavior of the input side of the step-down converter is of interest. These characteristics are important for the converter modeling in Section IV-C.

Fifth, it is assumed that the battery is adequately sized, such that both the power drawn from the loads and the power supplied by the solar PV have negligible effects on the behavior of the converters. These characteristics are important for the modeling of the converter behavior in Section IV-C.

III. CONTROL STRATEGY

In this section, the control strategy for swarm microgrids is developed. Intended to serve as a modular, *ad hoc* deployable, and highly scalable infrastructure, swarm microgrids are dc microgrids with special requirements in terms of control. As discussed in the first item in Section II-B, rapid deployment and ease of expansion are important attributes of a swarm microgrid. To attain these attributes, four main challenges related to the stability of swarm microgrids need to be addressed. First, the ability to scale the network must be

TABLE I
SUMMARY OF CONTROL STRATEGY FOR SWARM MICROGRIDS

Mode	Stability challenge to address	Control elements	Reference parameter
Supplying mode	#1 Ability to scale the network even at a varying number of units operating in supplying mode	Decentralized droop control	$v_{0,\text{ref},j}$, reference zero-current voltage;
	#2 Mitigation of oscillations between supplying converters	Low-pass filter (LPF) for droop control	$r_{\text{dr},j}$, reference droop resistance
Charging mode	#3 Ability to scale the network even at a varying number of units operating in charging mode	Power-drawing units involved in microgrid control	$i_{\text{n,ref},j}$, nodal current reference
	#4 Mitigation of constant power load (CPL) behavior	Nodal current control (CC)	

guaranteed, even at a varying number of power-supplying units. Second, oscillations between supplying converters need to be mitigated. Third, the ability to scale the network must be guaranteed, even at a varying number of power-drawing units. Fourth, CPL behavior, which can cause instability due to a negative resistance effect, needs to be mitigated.

The key principle underlying the control strategy for swarm microgrids is the involvement of all swarm units. Swarm units operating in both supplying and charging modes are involved in attaining the required stability. The four key challenges to maintaining stability in swarm dc microgrids are addressed by the following measures. First, measures undertaken in supplying mode are discussed. Second, measures undertaken in charging mode are presented. The control strategy is summarized in Table I and discussed as follows.

The supplying mode control scheme needs to ensure the ability to scale the network even at a varying number of units operating in supplying mode. This means ensuring a stable supply even when the number of supplying swarm units changes. This requirement implies that there must be a decentralized power sharing mechanism. Therefore, a mechanism for power sharing among the supplying swarm units needs to be implemented. This is accomplished by utilizing a current-based droop control scheme [12]

$$v_{\text{n,ref},j} = v_{0,\text{ref},j} - r_{\text{dr},j} \cdot i_{\text{n},j} \quad (1)$$

where $v_{\text{n,ref},j}$ is the reference node voltage, $v_{0,\text{ref},j}$ is the reference zero-current voltage, and $r_{\text{dr},j}$ is the droop resistance. The droop control scheme expressed in (1) follows a generic approach and can be further adapted as required for a specific deployment scenario, as presented, for example, in [42] and [43]. While the utilization of a current-based droop control scheme addresses the challenge of expandability, the second challenge must also be addressed. This challenge is to mitigate the risk of oscillations between supplying converters [18], [44]. To address this challenge, the droop control scheme needs to be extended through the addition of a low-pass filter (LPF) for $v_{\text{n,ref},j}$ of (1) to damp oscillations in the voltage reference. The introduction of an LPF into a droop control scheme has been demonstrated to address this stability challenge [45].

The main focus of the charging mode control scheme is to ensure the ability to scale the network even at a varying number of units operating in charging mode. This means ensuring stable operation of the microgrid even in situations

in which swarm units join the microgrid in an *ad hoc* manner. Therefore, a swarm unit in charging mode needs to be robust against perturbations and exhibit behavior that maintains the stability of the microgrid. Such robustness is achieved by involving not only the feeding units but also the power-drawing units in microgrid control. In particular, this means applying an active damping scheme at the swarm units operating in charging mode. This active damping scheme is designed to address the third challenge, namely, the risk of CPL behavior [32], [46]. To avoid the CPL effect, swarm units operating in charging mode apply active damping by directly controlling $i_{\text{n},j}$ in Fig. 2. This implementation is referred to as nodal current control (CC). This nodal CC is a reference tracking control scheme with the nodal current reference $i_{\text{n,ref},j}$. The implementation of nodal CC is possible, because a swarm unit operating in charging mode does not interface with any tightly controlled load. As shown in Fig. 2, a swarm unit operating in charging mode uses a step-down converter to charge a battery and does not directly supply power to any load. The reference parameter $i_{\text{n,ref},j}$ can be updated dynamically depending on the battery charging regime. Therefore, there are no restrictions on the implementation of the nodal CC scheme.

The reference parameters $v_{0,\text{ref},j}$, $r_{\text{dr},j}$, and $i_{\text{n,ref},j}$ are provided from an operational layer. In normal operation, these values change only at the intervals of seconds or minutes. A demonstration of the capacity to cater to changes in these reference parameters is part of the experimental validation in Section V. All discussed control provisions are summarized in Table I.

IV. SWARM MICROGRID MODELING

The objective of this section is to derive a mathematical model that allows for the representation and analysis of swarm microgrids of arbitrary sizes. The mathematical model derived here is then used in the subsequent sections to assess the stability of a swarm microgrid. To analyze the small-signal stability of the microgrid, a small-signal system model is required, as developed in this section. In particular, the small-signal model derived here is a linear time-invariant (LTI) model. To represent this system or parts of this system, the transfer function representation and state-space representation are used interchangeably [47]. The following convention is used: $x = X + \tilde{x}$, where X is the steady-state value, and \tilde{x} is the small-signal perturbation.

This section is structured as follows. Section IV-A describes the structure of the system model. Section IV-B gives the mathematical representation in terms of subsystems. Section IV-C presents the gray-box modeling approach used to model the behavior of the converters within the different subsystems. Section IV-D introduces the state-space representation of the consolidated microgrid system model by integrating the results from Sections IV-A–IV-C.

A. Structure of the System Model

The overall swarm microgrid is modeled as a multiple-input multiple-output system that consists of multiple subsystems. In turn, each of these subsystems consists of one or multiple transfer functions. System and subsystem definitions are denoted in the form Σ_{System} [47]. The swarm microgrid system

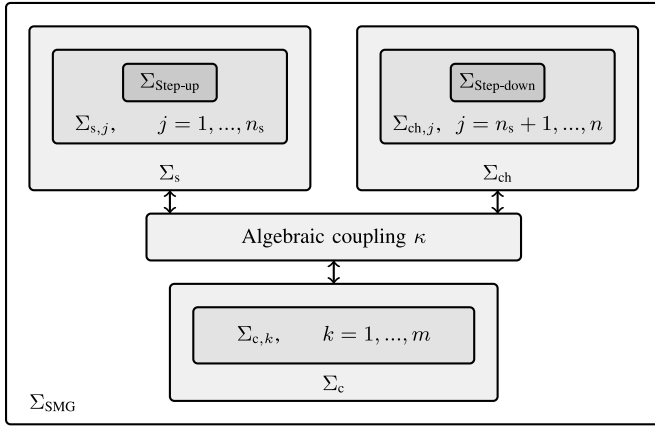


Fig. 3. Cascaded model of the swarm microgrid system Σ_{SMG} .

Σ_{SMG} is characterized by the system matrix \mathbf{A} , the input matrix \mathbf{B} , the output matrix \mathbf{C} , and the direct feedthrough matrix \mathbf{D} , as follows:

$$\Sigma_{SMG} : \begin{cases} \dot{\tilde{\mathbf{x}}} = \mathbf{A}\tilde{\mathbf{x}} + \mathbf{B}\tilde{\mathbf{u}} \\ \tilde{\mathbf{y}} = \mathbf{C}\tilde{\mathbf{x}} + \mathbf{D}\tilde{\mathbf{u}} \end{cases} \quad (2)$$

where $\tilde{\mathbf{x}}$ is the vector of the state variables, $\tilde{\mathbf{u}}$ is the vector of the control signals, and $\tilde{\mathbf{y}}$ is the output vector.

The system model Σ_{SMG} is derived in a cascaded manner, as shown in Fig. 3 and discussed as follows. The model consists of subsystems of distinct types. These subsystems represent the behavior of the swarm units and cables of the microgrid. As discussed in the third item in Section II-B, a swarm unit can operate in one of two modes: the supplying mode or the charging mode. Therefore, two types of subsystems are used to represent the swarm units.

- 1) A subsystem $\Sigma_{s,j}$ represents the behavior of swarm unit $j = 1, \dots, n_s$ operating in the supplying mode. A node operating in this mode uses a step-up converter. Therefore, the model of the step-up converter behavior $\Sigma_{Step-up}$ is an essential part of the model for the swarm units operating in the supplying mode. For concise mathematical representation, all swarm units operating in supplying mode are grouped into one aggregate subsystem Σ_s .
- 2) A subsystem $\Sigma_{ch,j}$ represents the behavior of swarm unit $j = n_s + 1, \dots, n$ operating in the charging mode. A node operating in this mode uses a step-down converter. Therefore, the model of the step-down converter behavior $\Sigma_{Step-down}$ is an essential part of the model for the swarm units operating in the charging mode. For concise mathematical representation, all swarm units operating in charging mode are grouped into one aggregate subsystem Σ_{ch} .

In addition, there is one subsystem type for cables.

- 1) A subsystem $\Sigma_{c,k}$ represents the behavior of cable $k = 1, \dots, m$. For concise mathematical representation, all cables are grouped into one aggregate subsystem Σ_c .

In total, the system consists of n_s swarm units in the supplying mode and $n - n_s$ swarm units in the charging mode. At any given time, each swarm unit can operate in only one of the two modes. Accordingly, the total number of swarm units is n .

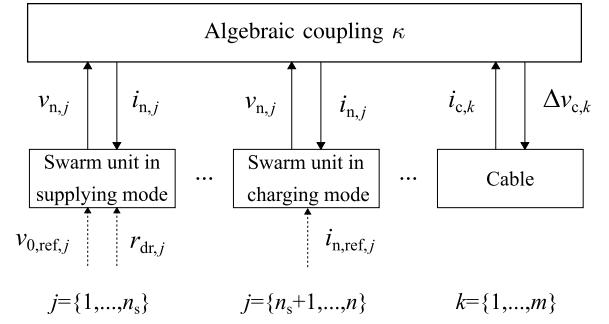


Fig. 4. Attributes and interrelation of the algebraically coupled subsystems.

The swarm units are connected by m cables. The indices j and k are used to identify swarm units and cables, respectively.

In summary, the cascaded system model is structured as follows:

$$\Sigma_{SMG} \supset \begin{cases} \Sigma_s \supset \Sigma_{s,j} \supset \Sigma_{Step-up} & \forall j = 1, \dots, n_s \\ \Sigma_{ch} \supset \Sigma_{ch,j} \supset \Sigma_{Step-down} & \forall j = n_s + 1, \dots, n \\ \Sigma_c \supset \Sigma_{c,k} & \forall k = 1, \dots, m \end{cases} \quad (3)$$

The different subsystem models are connected through an algebraic coupling κ . This concludes the description of the cascaded system model, as shown in Fig. 3.

B. Subsystem Attributes and Algebraic Coupling

This section derives the specific attributes of the three types of subsystems and their interactions through algebraic coupling. Mathematically, the algebraic coupling of the subsystems is expressed using the following conventions [47]. The algebraic coupling is represented by the coupling input vector $\tilde{\mathbf{s}}$, the coupling input matrix \mathbf{S} , the coupling output vector $\tilde{\mathbf{z}}$, and the coupling output matrix \mathbf{C}_z . Building on the overall system model in Fig. 3, the attributes of the subsystems are as shown in Fig. 4 and are discussed, from bottom to top, as follows.

Swarm units have internal controllers, which require the input of corresponding reference parameters. These reference parameters are represented by dashed arrows. The required reference parameters are given in Table I. For a swarm unit operating in the supplying mode, the reference parameters are the reference zero-current voltage $v_{0,ref,j}$ and the droop resistance $r_{dr,j}$. For a swarm unit operating in the charging mode, there is only one reference parameter, namely, the nodal current reference $i_{n,ref,j}$. There are no reference parameters for cable subsystem k .

The individual subsystems are coupled to each other. The solid arrows in Fig. 4 represent the coupling inputs and outputs of the subsystems. Each subsystem has one coupling input and one coupling output. For swarm unit j , the coupling input parameter is the nodal current $i_{n,j}$, and the coupling output parameter is the node voltage $v_{n,j}$. For cable k , the coupling input is the voltage difference $\Delta v_{c,k}$ between the two ends of the cable, and the coupling output is the current $i_{c,k}$ through the cable, as shown in Fig. 5.

The interconnections between the subsystems through the algebraic coupling κ are defined by the algebraic connection

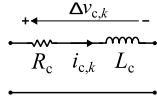


Fig. 5. Cable model with voltage difference $\Delta v_{c,k}$ between the two cable ends, resistance R_c , current $i_{c,k}$, and inductance L_c .

between the coupling input vector

$$s = \begin{bmatrix} \mathbf{i}_{n,s} \\ \mathbf{i}_{n,ch} \\ \Delta \mathbf{v}_c \end{bmatrix} \quad (4)$$

and the coupling output vector

$$z = \begin{bmatrix} \mathbf{v}_{n,s} \\ \mathbf{v}_{n,ch} \\ \mathbf{i}_c \end{bmatrix} \quad (5)$$

where the following hold.

- 1) $\mathbf{i}_{n,s}$ is the vector of all $i_{n,j}$ of all swarm units $j = 1, \dots, n_s$ in the supplying mode.
- 2) $\mathbf{i}_{n,ch}$ is the vector of all $i_{n,j}$ of all swarm units $j = n_s + 1, \dots, n$ in the charging mode.
- 3) $\Delta \mathbf{v}_c$ is the vector of all $\Delta v_{c,k}$ of all cables $k = 1, \dots, m$.
- 4) $\mathbf{v}_{n,s}$ is the vector of all $v_{n,j}$ of all swarm units $j = 1, \dots, n_s$ in the supplying mode.
- 5) $\mathbf{v}_{n,ch}$ is the vector of all $v_{n,j}$ of all swarm units $j = n_s + 1, \dots, n$ in the charging mode.
- 6) \mathbf{i}_c is the vector of all $i_{c,k}$ of all cables $k = 1, \dots, m$.

To establish the algebraic coupling κ between the subsystem models, the topology-specific incidence matrix \mathbf{M} is used. Any arbitrary topology can be represented by means of a corresponding configuration of \mathbf{M} [15], [48]. The elements of \mathbf{M} take the values of -1 , 0 , and 1 . The incidence matrix \mathbf{M} establishes the relationship between the nodal currents and the cable currents, such that

$$\begin{bmatrix} \mathbf{i}_{n,s} \\ \mathbf{i}_{n,ch} \end{bmatrix} = \mathbf{M}^T \cdot \mathbf{i}_c \quad (6)$$

and the relationship between the node voltages and the voltage drops across the cables, such that

$$\Delta \mathbf{v}_c = \mathbf{M} \cdot \begin{bmatrix} \mathbf{v}_{n,s} \\ \mathbf{v}_{n,ch} \end{bmatrix}. \quad (7)$$

The incidence matrix \mathbf{M} is further separated into two submatrices

$$\mathbf{M} = [\mathbf{M}_s \quad \mathbf{M}_{ch}] \quad (8)$$

where \mathbf{M}_s represents the coupling of cables to nodes operating in the supplying mode, and \mathbf{M}_{ch} represents the coupling of cables to swarm units operating in the charging mode. Then, following Fig. 4, the algebraic coupling κ is expressed as:

$$\kappa : \underbrace{\begin{bmatrix} \mathbf{i}_{n,s} \\ \mathbf{i}_{n,ch} \\ \Delta \mathbf{v}_c \end{bmatrix}}_{=s} = \begin{bmatrix} \mathbf{0} & \mathbf{0} & \mathbf{M}_s^T \\ \mathbf{0} & \mathbf{0} & \mathbf{M}_{ch}^T \\ \mathbf{M}_s & \mathbf{M}_{ch} & \mathbf{0} \end{bmatrix} \underbrace{\begin{bmatrix} \mathbf{v}_{n,s} \\ \mathbf{v}_{n,ch} \\ \mathbf{i}_c \end{bmatrix}}_{=z}. \quad (9)$$

C. Gray-Box Modeling Within Subsystems

As shown in the system model in Fig. 3 and according to (3), an important part of each subsystem model is the representation of the converters of the corresponding swarm unit, as depicted in Fig. 2. The behaviors of both the step-up converter and the step-down converter need to be modeled. As discussed in the third item in Section II-B, a swarm unit can operate in only one of the two modes at any given time. Therefore, a distinct model for the step-up converter behavior in the supplying mode and a distinct model for the step-down converter behavior in the charging mode are developed. To achieve a realistic representation for the stability analysis in Section VI, a gray-box modeling approach is followed.

Gray-box modeling refers to an approach in which parts of the system are modeled based on ideal behavior, and other parts are modeled based on measurements and, therefore, real behavior [49]. In the gray-box model derived here, only one component is modeled with ideal behavior. This component is the input capacitor, which is modeled as an ideal capacitor without parasitic resistance. This is done to account for the worst case from a stability perspective, because the parasitic resistance of a capacitor exerts a known stabilizing effect [50]. The other components of the gray-box model are derived from measurements, building on the existing literature on black-box converter modeling [34], [35], [37].

In the black-box converter modeling literature, a converter behavior is typically modeled using an unterminated two-port model [37] with three types of components. First, the input admittance and output impedance of the converter are included. Second, two transfer functions, named the audio susceptibility and the back current gain, account for the influence between the input and output quantities. Third, the model may include additional transfer functions related to reference tracking [36].

The model derived here is distinctly different, mainly because the converters are not unterminated but rather terminate at a battery on one side, as shown in Fig. 2. This battery termination allows for the model to be notably simplified by modeling the closed-loop behavior of the combined system of battery and converter. Because the internal behavior is reflected in the closed-loop behavior of this combined system, the internal transfer functions of the converter mentioned earlier, the audio susceptibility and the back current gain, can be omitted. The remainder of the model needs to accurately represent the behavior of the active components in either mode. The active components of a swarm unit operating in the supplying mode are shown in Fig. 6(a), and the active components of a swarm unit operating in the charging mode are shown in Fig. 6(b).

As discussed in the fifth item in Section II-B, the influences of the load and solar PV on the battery are regarded as negligible from a network stability point of view. Therefore, the converter models here can focus solely on the behavior of the swarm-node-facing side. As stated in the fourth item in Section II-B, the swarm-node-facing side is the output side of the step-up converter and the input side of the step-down converter.

The model boundaries, shown as dashed lines in Fig. 6(a) and (b), encompass both the converter and the battery. The small-signal models for the step-up and step-down

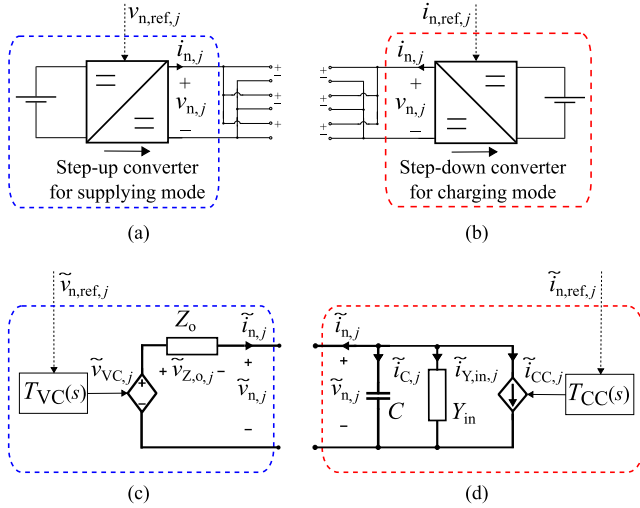


Fig. 6. Active components of a swarm unit when operating in (a) supplying mode and (b) charging mode, where the system model boundaries are shown by dashed lines; equivalent circuits of the small-signal models for the converter output behavior when operating in (c) supplying mode and (d) charging mode.

converter behaviors are presented subsequently in that order. The reader is reminded that the following convention is used: $x = X + \tilde{x}$, where X is the steady-state value, and \tilde{x} is the small-signal perturbation.

1) *Step-Up Converter Behavior Modeling*: The step-up converter behavior model encompasses the battery of the swarm unit and the step-up converter, as shown in Fig. 6(a). This model needs to describe the change in the node voltage $\tilde{v}_{n,j}$ due to either a change in the nodal current $\tilde{i}_{n,j}$ that it is supplying or a change in the reference node voltage $\tilde{v}_{n,ref,j}$

$$\tilde{v}_{n,j} = -\tilde{v}_{Z_o,j} + \tilde{v}_{VC,j} \quad (10)$$

where the quantity $\tilde{v}_{Z_o,j}$ represents the change in response to a change in the nodal current $\tilde{i}_{n,j}$ due to the output impedance $Z_o(s)$

$$Z_o(s) = \frac{\tilde{v}_{Z_o,j}}{\tilde{i}_{n,j}} \quad (11)$$

In addition, the converter-internal output voltage control (VC) to control the node voltage is included. This is accomplished by including the transfer function $T_{VC}(s)$, which models the response of $\tilde{v}_{VC,j}$ to changes in the reference node voltage $\tilde{v}_{n,ref,j}$

$$T_{VC}(s) = \frac{\tilde{v}_{VC,j}}{\tilde{v}_{n,ref,j}} \quad (12)$$

The combined small-signal model for the step-up converter behavior is shown in Fig. 6(c) and summarized as follows:

$$\Sigma_{\text{Step-up}} : \left\{ \tilde{v}_{n,j} = -Z_o(s) \cdot \tilde{i}_{n,j} + T_{VC}(s) \cdot \tilde{v}_{n,ref,j} \right. \quad (13)$$

2) *Step-Down Converter Behavior Modeling*: The step-down converter behavior model encompasses the battery of the swarm unit and the step-down converter, as shown in Fig. 6(b). This model needs to describe the change in the node voltage $\tilde{v}_{n,j}$ due to either a change in the nodal current reference $\tilde{i}_{n,ref,j}$ or a change in the nodal current $\tilde{i}_{n,j}$.

The behavior due to changes in the nodal current $\tilde{i}_{n,j}$ is modeled through a combination of the input admittance and an explicit model of the input capacitor. As described earlier in this section, when introducing the gray-box modeling

approach, an ideal capacitor model is used to account for the worst case scenario from a stability point of view. Following the ideal capacitor model and considering a capacitance C

$$T_C(s) = \frac{1}{C \cdot s} \quad (14)$$

The transfer function $T_C(s)$ describes the behavior of the node voltage $\tilde{v}_{n,j}$ in response to changes in the capacitor current $\tilde{i}_{C,j}$

$$T_C(s) = \frac{\tilde{v}_{n,j}}{\tilde{i}_{C,j}} \quad (15)$$

Changes in the capacitor current depend on changes in the nodal current $\tilde{i}_{n,j}$, in $\tilde{i}_{Y,in,j}$, and in $\tilde{i}_{CC,j}$, as follows:

$$\tilde{i}_{C,j} = -\tilde{i}_{n,j} - \tilde{i}_{Y,in,j} - \tilde{i}_{CC,j} \quad (16)$$

where $\tilde{i}_{Y,in,j}$ represents changes that originate from changes in the node voltage $\tilde{v}_{n,j}$ due to the input admittance $Y_{in}(s)$

$$Y_{in}(s) = \frac{\tilde{i}_{Y,in,j}}{\tilde{v}_{n,j}} \quad (17)$$

Furthermore, converter-internal input CC to control the nodal current is modeled. In particular, the response of $\tilde{i}_{CC,j}$ to changes in the nodal current reference $\tilde{i}_{n,ref,j}$ is modeled by the transfer function $T_{CC}(s)$

$$T_{CC}(s) = \frac{\tilde{i}_{CC,j}}{\tilde{i}_{n,ref,j}} \quad (18)$$

The combined small-signal model for the step-down converter behavior is shown in Fig. 6(d) and summarized as follows:

$$\Sigma_{\text{Step-down}} : \left\{ \begin{aligned} \tilde{v}_{n,j} &= T_C(s) \cdot \tilde{i}_{C,j} \\ \tilde{i}_{C,j} &= -\tilde{i}_{n,j} - Y_{in}(s) \cdot \tilde{v}_{n,j} - T_{CC}(s) \cdot \tilde{i}_{n,ref,j} \end{aligned} \right. \quad (19)$$

3) *Transfer Function Identification*: The converter behavior models in (13) and (19) rely on the experimental identification of the black-box behavior transfer functions $Z_o(s)$, $T_{VC}(s)$, $Y_{in}(s)$, and $T_{CC}(s)$. These four transfer functions are LTI models that follow a generic structure, consisting of the sum of a first-order subsystem and a second-order subsystem [35]:

$$T(s) = \underbrace{\frac{K_1}{1 + T_1 \cdot s}}_{\text{First-order subsystem}} + \underbrace{\frac{K_2(1 + T_{\text{zero}} \cdot s)}{1 + 2 \cdot \zeta \cdot T_2 \cdot s + (T_2 \cdot s)^2}}_{\text{Second-order subsystem}} \quad (20)$$

where the following hold.

- 1) K_1 is the proportional gain of the first-order subsystem.
- 2) T_1 is the time constant associated with the pole of the first-order subsystem.
- 3) K_2 is the proportional gain of the second-order subsystem.
- 4) T_{zero} is the time constant associated with the transfer function zero of the second-order subsystem.
- 5) ζ is the damping factor of the second-order subsystem.
- 6) T_2 is the time constant associated with the double pole pair of the second-order subsystem.

The detailed black-box transfer functions and identified parameter values are based on experimental data. These data and parameter identification results are provided in Appendix C.

It should be noted that if the converter behavior cannot be described by a model with the generic form of (20), then higher-order transfer functions need to be used. Examples for such higher-order transfer functions are discussed in [35].

D. State-Space Representation

The overall model of the swarm microgrid system Σ_{SMG} , as given in (3), contains three types of subsystem models. As shown in Fig. 3, these three subsystem model types correspond to 1) a swarm unit operating in the supplying mode, $\Sigma_{s,j}$; 2) a swarm unit operating in the charging mode, $\Sigma_{\text{ch},j}$; and 3) a cable, $\Sigma_{c,k}$. These models are defined as follows.

1) *Node Model for the Supplying Mode:* Based on Fig. 4 and Table I, the subsystem model for a swarm unit operating in the supplying mode, $\Sigma_{s,j}$, is developed in three steps. First, the input and output definitions of Fig. 4 are used.

Therefore, the control vector is $\tilde{\mathbf{u}}_{s,j} = \begin{bmatrix} \tilde{v}_{0,\text{ref},j} \\ \tilde{r}_{\text{dr},j} \end{bmatrix}$, the coupling input is $\tilde{s}_{s,j} = \tilde{i}_{n,j}$, the subsystem output is $\tilde{y}_{s,j} = \tilde{v}_{n,j}$, and the coupling output is $\tilde{z}_{s,j} = \tilde{v}_{n,j}$. Second, the droop control scheme expressed in (1) with an LPF, as indicated in Table I, is incorporated. This LPF is characterized by the filter frequency f_{LPF} . The droop equation (1) is linearized around the steady-state values $I_{n,j}$ and $R_{\text{dr},j}$. Third, the step-up converter shown in Fig. 2 is represented by an output-side-only model, as discussed in Section IV-C. The output behavior of the step-up converter is modeled according to (13) using the output-side transfer functions $Z_o(s)$ and $T_{\text{VC}}(s)$. These three steps result in the supplying mode swarm unit model, which is shown in Fig. 7 and is defined as follows:

$$\Sigma_{s,j} : \left\{ \begin{array}{l} \dot{\tilde{\mathbf{x}}}_{s,j} = \underbrace{\begin{bmatrix} -f_{\text{LPF}} & \mathbf{0} & \mathbf{0} \\ \mathbf{B}_{\text{VC}} & \mathbf{A}_{\text{VC}} & \mathbf{0} \\ \mathbf{0} & \mathbf{0} & \mathbf{A}_{\text{Zo}} \end{bmatrix}}_{=\mathbf{A}_{s,j}} \cdot \underbrace{\begin{bmatrix} \tilde{v}_{n,\text{ref},j} \\ \tilde{\mathbf{x}}_{\text{VC},j} \\ \tilde{\mathbf{x}}_{\text{Zo},j} \end{bmatrix}}_{=\tilde{\mathbf{x}}_{s,j}} \\ + \underbrace{\begin{bmatrix} f_{\text{LPF}} & -I_{n,j} \cdot f_{\text{LPF}} \\ \mathbf{0} & \mathbf{0} \\ \mathbf{0} & \mathbf{0} \end{bmatrix}}_{=\mathbf{B}_{s,j}} \cdot \underbrace{\begin{bmatrix} \tilde{v}_{0,\text{ref},j} \\ \tilde{r}_{\text{dr},j} \end{bmatrix}}_{=\tilde{\mathbf{u}}_{s,j}} \\ + \underbrace{\begin{bmatrix} -R_{\text{dr},j} \cdot f_{\text{LPF}} & \\ \mathbf{0} & \mathbf{B}_{\text{Zo}} \end{bmatrix}}_{=\mathbf{S}_{s,j}} \cdot \underbrace{\begin{bmatrix} \tilde{i}_{n,j} \end{bmatrix}}_{=\tilde{s}_{s,j}} \\ \tilde{v}_{n,j} = \underbrace{\begin{bmatrix} 0 & \mathbf{C}_{\text{VC}} & -\mathbf{C}_{\text{Zo}} \end{bmatrix}}_{=\mathbf{C}_{s,j}} \cdot \tilde{\mathbf{x}}_{s,j} \\ \tilde{v}_{n,j} = \underbrace{\begin{bmatrix} 0 & \mathbf{C}_{\text{VC}} & -\mathbf{C}_{\text{Zo}} \end{bmatrix}}_{=\mathbf{C}_{z,s,j}} \cdot \tilde{\mathbf{x}}_{s,j} \\ \mathbf{D}_{s,j} = \mathbf{0} \end{array} \right. \quad (21)$$

where the following hold.

- 1) $\tilde{\mathbf{x}}_{s,j}$ is the vector of the state variables for swarm unit j operating in the supplying mode.
- 2) \mathbf{A}_{VC} , \mathbf{B}_{VC} , \mathbf{C}_{VC} , and $\tilde{\mathbf{x}}_{\text{VC},j}$ give the state-space representation of $T_{\text{VC}}(s)$.

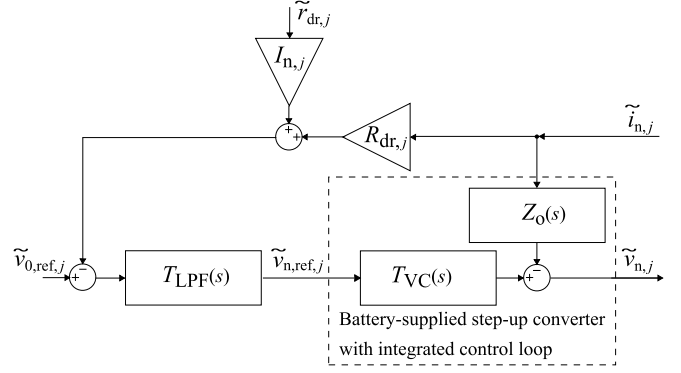


Fig. 7. Linearized small-signal model for a swarm unit operating in the supplying mode, $\Sigma_{s,j}$.

- 3) \mathbf{A}_{Zo} , \mathbf{B}_{Zo} , \mathbf{C}_{Zo} , and $\tilde{\mathbf{x}}_{\text{Zo},j}$ give the state-space representation of $Z_o(s)$.

- 4) $\mathbf{A}_{s,j}$ is the system matrix, $\mathbf{B}_{s,j}$ is the control matrix, $\mathbf{C}_{s,j}$ is the output matrix, $\mathbf{D}_{s,j}$ is the direct feedthrough matrix, $\mathbf{S}_{s,j}$ is the coupling input matrix, and $\mathbf{C}_{z,s,j}$ is the coupling output matrix of the subsystem for swarm unit j operating in the supplying mode.

2) *Node Model for the Charging Mode:* Based on Fig. 4 and Table I, the subsystem model for a swarm unit operating in the charging mode, $\Sigma_{\text{ch},j}$, is also developed in three steps. As for the supplying mode, first, the input and output definitions of Fig. 4 are used. Therefore, the control input is $\tilde{\mathbf{u}}_{\text{ch},j} = \tilde{i}_{n,\text{ref},j}$, the coupling input is $\tilde{s}_{\text{ch},j} = \tilde{i}_{n,j}$, the subsystem output is $\tilde{y}_{\text{ch},j} = \tilde{v}_{n,j}$, and the coupling output is $\tilde{z}_{\text{ch},j} = \tilde{v}_{n,j}$. Second, the nodal CC scheme listed in Table I is incorporated. Third, the step-down converter shown in Fig. 2 is represented by an input-side-only model, as discussed in Section IV-C. The input behavior of the step-down converter is modeled according to (19) using the input-side transfer functions $T_{\text{C}}(s)$, $Y_{\text{in}}(s)$, and $T_{\text{CC}}(s)$. As described in Section IV-C, the capacitor is modeled as an ideal capacitor with capacitance C according to (14). The abovementioned steps result in the charging mode swarm unit model, which is shown in Fig. 8 and is defined as follows:

$$\Sigma_{\text{ch},j} : \left\{ \begin{array}{l} \dot{\tilde{\mathbf{x}}}_{\text{ch},j} = \underbrace{\begin{bmatrix} \mathbf{0} & -C_{\text{CC}}/C & -C_{\text{Yin}}/C \\ \mathbf{0} & \mathbf{A}_{\text{CC}} & \mathbf{0} \\ \mathbf{B}_{\text{Yin}} & \mathbf{0} & \mathbf{A}_{\text{Yin}} \end{bmatrix}}_{=\mathbf{A}_{\text{ch},j}} \cdot \underbrace{\begin{bmatrix} \tilde{v}_{n,j} \\ \tilde{\mathbf{x}}_{\text{CC},j} \\ \tilde{\mathbf{x}}_{\text{Yin},j} \end{bmatrix}}_{=\tilde{\mathbf{x}}_{\text{ch},j}} \\ + \underbrace{\begin{bmatrix} \mathbf{0} \\ \mathbf{B}_{\text{CC}} \\ \mathbf{0} \end{bmatrix}}_{=\mathbf{B}_{\text{ch},j}} \cdot \underbrace{\begin{bmatrix} \tilde{i}_{n,\text{ref},j} \end{bmatrix}}_{=\tilde{\mathbf{u}}_{\text{ch},j}} + \underbrace{\begin{bmatrix} -1/C \\ \mathbf{0} \\ \mathbf{0} \end{bmatrix}}_{=\mathbf{S}_{\text{ch},j}} \cdot \underbrace{\begin{bmatrix} \tilde{i}_{n,j} \end{bmatrix}}_{=\tilde{s}_{\text{ch},j}} \\ \tilde{v}_{n,j} = \underbrace{\begin{bmatrix} 1 & \mathbf{0} & \mathbf{0} & \mathbf{0} \end{bmatrix}}_{=\mathbf{C}_{\text{ch},j}} \cdot \tilde{\mathbf{x}}_{\text{ch},j} \\ \tilde{v}_{n,j} = \underbrace{\begin{bmatrix} 1 & \mathbf{0} & \mathbf{0} & \mathbf{0} \end{bmatrix}}_{=\mathbf{C}_{z,\text{ch},j}} \cdot \tilde{\mathbf{x}}_{\text{ch},j} \\ \mathbf{D}_{\text{ch},j} = \mathbf{0} \end{array} \right. \quad (22)$$

where the following hold.

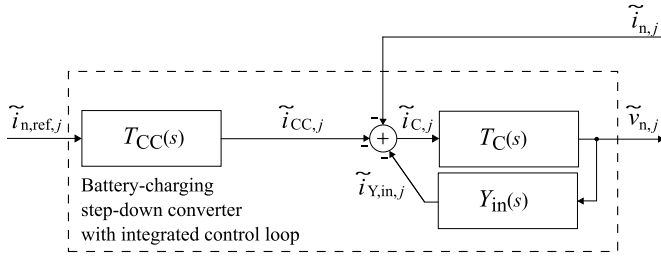


Fig. 8. Linearized small-signal model for a swarm unit operating in the charging mode, $\Sigma_{ch,j}$.

- 1) $\tilde{\mathbf{x}}_{ch,j}$ is the vector of the state variables for swarm unit j operating in the charging mode.
- 2) \mathbf{A}_{CC} , \mathbf{B}_{CC} , \mathbf{C}_{CC} , and $\tilde{\mathbf{x}}_{CC,j}$ give the state-space representation of $T_{CC}(s)$.
- 3) \mathbf{A}_{Yin} , \mathbf{B}_{Yin} , \mathbf{C}_{Yin} , and $\tilde{\mathbf{x}}_{Yin,j}$ give the state-space representation of $Y_{in}(s)$.
- 4) $\mathbf{A}_{ch,j}$ is the system matrix, $\mathbf{B}_{ch,j}$ is the control matrix, $\mathbf{C}_{ch,j}$ is the output matrix, $\mathbf{D}_{ch,j}$ is the direct feedthrough matrix, $\mathbf{S}_{ch,j}$ is the coupling input matrix, and $\mathbf{C}_{z,ch,j}$ is the coupling output matrix of the subsystem for swarm unit j operating in the charging mode.

3) *Cable Model*: Based on Fig. 4, the cable model $\Sigma_{c,k}$ is developed in two steps. First, the input and output definitions of Fig. 4 are used. Therefore, the coupling input is $\tilde{s}_{c,j} = \Delta \tilde{v}_{c,k}$, the subsystem output is $\tilde{y}_{c,j} = \tilde{i}_{c,k}$, and the coupling output is $\tilde{z}_{c,j} = \tilde{i}_{c,k}$. There is no control vector. Second, the cable model comprises inductive and resistive elements, as shown in Fig. 5. The line equation is given as follows:

$$\Delta \tilde{v}_{c,k} = L_c \cdot \dot{\tilde{i}}_{c,k} + R_c \cdot \tilde{i}_{c,k} \quad (23)$$

where R_c is the cable resistance, and L_c is the cable inductance. The length l_c , the conductivity σ_c , and the cross-sectional area A_c of the cable are considered

$$R_c = \frac{2 \cdot l_c}{\sigma_c \cdot A_c}. \quad (24)$$

The full model of the subsystem corresponding to cable k with state vector $\tilde{\mathbf{x}}_{c,k}$ is expressed as follows:

$$\Sigma_{c,k} : \begin{cases} \dot{\tilde{\mathbf{x}}}_{c,k} = \underbrace{\begin{bmatrix} -R_{c,k} \\ L_{c,k} \end{bmatrix}}_{=\mathbf{A}_{c,k}} \cdot \underbrace{\begin{bmatrix} \tilde{i}_{c,k} \end{bmatrix}}_{=\tilde{\mathbf{x}}_{c,k}} + \underbrace{\begin{bmatrix} 1 \\ L_{c,k} \end{bmatrix}}_{=\mathbf{S}_{c,k}} \cdot \underbrace{\begin{bmatrix} \Delta \tilde{v}_{c,k} \end{bmatrix}}_{=\tilde{s}_{c,k}} \\ \tilde{i}_{c,k} = \underbrace{\begin{bmatrix} 1 \end{bmatrix}}_{=\mathbf{C}_{c,k}} \cdot \tilde{\mathbf{x}}_{c,k} \\ \tilde{i}_{c,k} = \underbrace{\begin{bmatrix} 1 \end{bmatrix}}_{=\mathbf{C}_{c,k}} \cdot \tilde{\mathbf{x}}_{c,k} \\ \tilde{z}_{c,k} = \underbrace{\begin{bmatrix} 1 \end{bmatrix}}_{=\mathbf{C}_{c,k}} \cdot \tilde{\mathbf{x}}_{c,k} \\ \mathbf{B}_{c,k} = \mathbf{0}, \quad \mathbf{D}_{c,k} = \mathbf{0} \end{cases} \quad (25)$$

where $\mathbf{A}_{c,k}$ is the system matrix, $\mathbf{B}_{c,k}$ is the control matrix, $\mathbf{C}_{c,k}$ is the output matrix, $\mathbf{D}_{c,k}$ is the direct feedthrough matrix, $\mathbf{S}_{c,k}$ is the coupling input matrix, and $\mathbf{C}_{z,c,k}$ is the coupling output matrix of the subsystem for cable k . Note that vector and matrix notation is maintained even for the scalar quantities in (25). This is done to maintain coherence with (21)

and (22) and to facilitate clear referencing when combining the subsystems into the system model in Section IV-D4 as follows.

4) *Combined System Model*: To construct the overall system model, the definitions derived throughout Section IV are combined. The overall cascaded system model definition according to (3) and Fig. 3 is followed. The individual subsystem definitions for $\Sigma_{s,j}$ in (21), $\Sigma_{ch,j}$ in (22), and $\Sigma_{c,k}$ in (25) are used.

In accordance with (3), the individual subsystem definitions are aggregated according to their types: Σ_s , Σ_{ch} , and Σ_c . This means that all vectors, namely, $\tilde{\mathbf{x}}_s$, $\tilde{\mathbf{x}}_{ch}$, $\tilde{\mathbf{x}}_c$, $\tilde{\mathbf{u}}_s$, and $\tilde{\mathbf{u}}_{ch}$, are combined vectors of the respective quantities corresponding to the individual subsystems. For example, $\tilde{\mathbf{x}}_s$ is a vector of all $\tilde{\mathbf{x}}_{s,j}$. Furthermore, all obtained matrices, namely, \mathbf{A}_s , \mathbf{A}_{ch} , \mathbf{A}_c , \mathbf{B}_s , \mathbf{B}_{ch} , \mathbf{C}_s , \mathbf{C}_{ch} , \mathbf{C}_c , $\mathbf{C}_{z,s}$, $\mathbf{C}_{z,ch}$, $\mathbf{C}_{z,c}$, \mathbf{S}_s , \mathbf{S}_{ch} , and \mathbf{S}_c , possess a diagonal structure consisting of the respective quantities of the individual subsystems. For example, \mathbf{A}_s is the system matrix for all swarm units operating in the supplying mode and is constructed using the elements of $\mathbf{A}_{s,j}$ in a diagonal form. The algebraic coupling definition of (9) is used to connect the submodels to each other. Thus, the overall system model is derived as follows:

$$\Sigma_{SMG} : \begin{cases} \dot{\tilde{\mathbf{x}}} = \underbrace{\begin{bmatrix} \mathbf{A}_s & \mathbf{0} & \mathbf{S}_s \mathbf{M}_s^T \mathbf{C}_{z,c} \\ \mathbf{0} & \mathbf{A}_{ch} & \mathbf{S}_{ch} \mathbf{M}_{ch}^T \mathbf{C}_{z,c} \\ \mathbf{S}_c \mathbf{M}_s \mathbf{C}_{z,s} & \mathbf{S}_c \mathbf{M}_{ch} \mathbf{C}_{z,ch} & \mathbf{A}_c \end{bmatrix}}_{=\mathbf{A}} \cdot \underbrace{\begin{bmatrix} \tilde{\mathbf{x}}_s \\ \tilde{\mathbf{x}}_{ch} \\ \tilde{\mathbf{x}}_c \end{bmatrix}}_{=\tilde{\mathbf{x}}} + \underbrace{\begin{bmatrix} \mathbf{B}_s & \mathbf{0} \\ \mathbf{0} & \mathbf{B}_{ch} \\ \mathbf{0} & \mathbf{0} \end{bmatrix}}_{=\mathbf{B}} \cdot \underbrace{\begin{bmatrix} \tilde{\mathbf{u}}_s \\ \tilde{\mathbf{u}}_{ch} \end{bmatrix}}_{=\tilde{\mathbf{u}}} \\ \underbrace{\begin{bmatrix} \tilde{v}_{n,s} \\ \tilde{v}_{n,ch} \\ \tilde{i}_{n,s} \\ \tilde{i}_{n,ch} \end{bmatrix}}_{=\tilde{\mathbf{y}}} = \underbrace{\begin{bmatrix} \mathbf{C}_s & \mathbf{0} & \mathbf{0} \\ \mathbf{0} & \mathbf{C}_{ch} & \mathbf{0} \\ \mathbf{0} & \mathbf{0} & \mathbf{M}_s^T \mathbf{C}_c \\ \mathbf{0} & \mathbf{0} & \mathbf{M}_{ch}^T \mathbf{C}_c \end{bmatrix}}_{=\mathbf{C}} \cdot \tilde{\mathbf{x}} \\ \mathbf{D} = \mathbf{0} \end{cases} \quad (26)$$

V. EXPERIMENTAL VALIDATION

In this section, the swarm microgrid model developed in Section IV is validated in a laboratory environment. The objective of this validation is to demonstrate the accurate modeling of the system. Experimental data are compared with simulation results on the basis of the LTI model. The model validation criteria are threefold. First, the simulation output should match the experimental data. In particular, any mismatches due to ripples should be less than 10% of the average values. Second, the model response should be especially accurate to changes in the reference values with waveforms similar to those observed in the experimental setup. Third, the model must adequately represent spikes and rapid changes, particularly after increases in the power drawn by any swarm unit.

To compare the simulation results of the LTI model with the experimental data, the steady-state values need to be

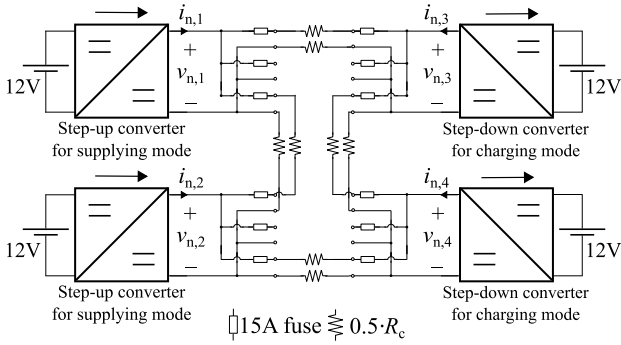


Fig. 9. Laboratory setup for microgrid validation with $n = 4$.

determined. As in Section IV, the following convention is used: $x = X + \tilde{x}$, where X is the steady-state value, and \tilde{x} is the small-signal perturbation. The steady-state equations for a swarm microgrid are given in Appendix B. The remainder of this section is divided into two parts. First, the experimental design is presented; second, the obtained results are discussed.

A. Experimental Design

The experimental setup is depicted in Fig. 9. Swarm units $j = 1$ and $j = 2$ are operating in the supplying mode using step-up converters. Swarm units $j = 3$ and $j = 4$ are operating in the charging mode using step-down converters. All three relevant types of interactions are present in the chosen topology: 1) interactions between neighboring swarm units in the supplying mode; 2) interactions between neighboring swarm units in the charging mode; and 3) interactions between neighboring swarm units in different modes.

The values of the model parameters are provided in the third column of Table III presented in Section VI-C. The parameters related to the cable resistances are chosen such that utilization of standard laboratory equipment is possible. The only deviation from the parameter values provided in Table III is the steady-state nodal current reference $I_{n,ref,j}$, for which the reference values are $I_{n,ref,3} = -1$ A and $I_{n,ref,4} = -0.8$ A. As such, the two swarm units operating in the charging mode have two different steady-state reference current values, and the waveforms are clearly distinguishable.

Details on the laboratory equipment used and the parameter identification for the converter behavior are provided in Appendix C. To demonstrate the coherence of the model and the experimental behavior, three perturbations are applied to the system: 1) an increase and a subsequent decrease in $r_{dr,j}$ for swarm unit $j = 1$, at $t = 0.2$ s and $t = 0.3$ s, respectively; 2) an increase and a subsequent decrease in $v_{0,ref,j}$ for swarm unit $j = 1$, at $t = 0.4$ s and $t = 0.5$ s, respectively; and 3) a decrease and a subsequent increase in $i_{n,ref,j}$ for swarm unit $j = 3$, at $t = 0.6$ s and $t = 0.7$ s, respectively.

B. Comparison of Model-Derived Simulations and Experimental Results

The laboratory results are presented in Fig. 10. The first and third plots from the top show the corresponding laboratory (lab) data for the node voltages $v_{n,j}$ and the nodal currents $i_{n,j}$, respectively. The second and fourth plots show

the simulation (sim) results for the same quantities obtained using the LTI model derived in (26). In the following, an assessment in accordance with the three validation criteria defined earlier is undertaken.

The results of the LTI model generally resemble the real-world behavior well. The highest ripple content is present at unit $j = 3$ between between $t = 0.6$ s and $t = 0.7$ s, when the highest current is drawn from the network. The voltage ripples are less than 2 V in amplitude. This corresponds to a ripple content of less than 3%. The current ripples are less than 0.1 A in amplitude. This corresponds to a ripple content of less than 6%. In both cases, the ripple content is less than 10%. Therefore, the first validation criterion is fulfilled.

Furthermore, the behavior in response to changes in the reference values is well modeled, thus also fulfilling the second validation criterion. First, an increase in $r_{dr,1}$ causes a decrease in $v_{n,1}$, as in (1). Second, an increase in $v_{0,ref,1}$ results in an increase in $v_{n,1}$, as in (1). The two swarm units operating in the supplying mode share the load following the droop equation (1). Changes to the reference parameters in the droop control scheme are visible in the resulting effects on the current sharing characteristics. For example, as $r_{dr,1}$ increases between $t = 0.2$ s and $t = 0.3$ s, $i_{n,1}$ decreases, whereas $i_{n,2}$ increases. Third, the nodal current at swarm unit $j = 3$ is directly controlled through $i_{n,ref,3}$.

The waveforms after the corresponding increase and decrease in the power drawn from the network are accurately modeled, particularly the waveforms of the spikes. Therefore, the third validation criterion is also fulfilled.

VI. STABILITY ANALYSIS

In this section, the stability of a swarm microgrid is analyzed to demonstrate its expandability. Expandability up to $n = 1000$ is defined as a core requirement for swarm microgrids, as discussed in the second item in Section II-B. Building on the practical validation for a swarm microgrid of size $n = 4$ in Section V, this section demonstrates the results of increasing the quantity of swarm units to $n = 1000$. As laboratory validation is no longer feasible at this scale, the LTI model is utilized. The modeling approach derived in Section IV is used to scale the model up to a large microgrid. The generic topology shown in Fig. 11(b) is used. In the first part of this section, a qualitative assessment of stability is undertaken, followed by a detailed quantitative analysis including single-parameter variation and two-parameter variation.

A. Qualitative Assessment of Stability

Before the stability of the system is assessed quantitatively, this section first undertakes a brief qualitative assessment. The method is inspired by the assessment of the relationships between species in a given ecosystem [51]. When assessing such an ecosystem, the interactions between different species are captured with fundamental types of relationships, such as competition and mutualism. Similarly, the relationships between state variables of a microgrid model can be assessed [51]. For this assessment, the elements $a_{hg} \in A$ of the system matrix A defined in (26) are analyzed. Two qualitative robustness metrics as discussed in [51] and [52] are used. Both metrics are defined, such that a low value indicates a high robustness.

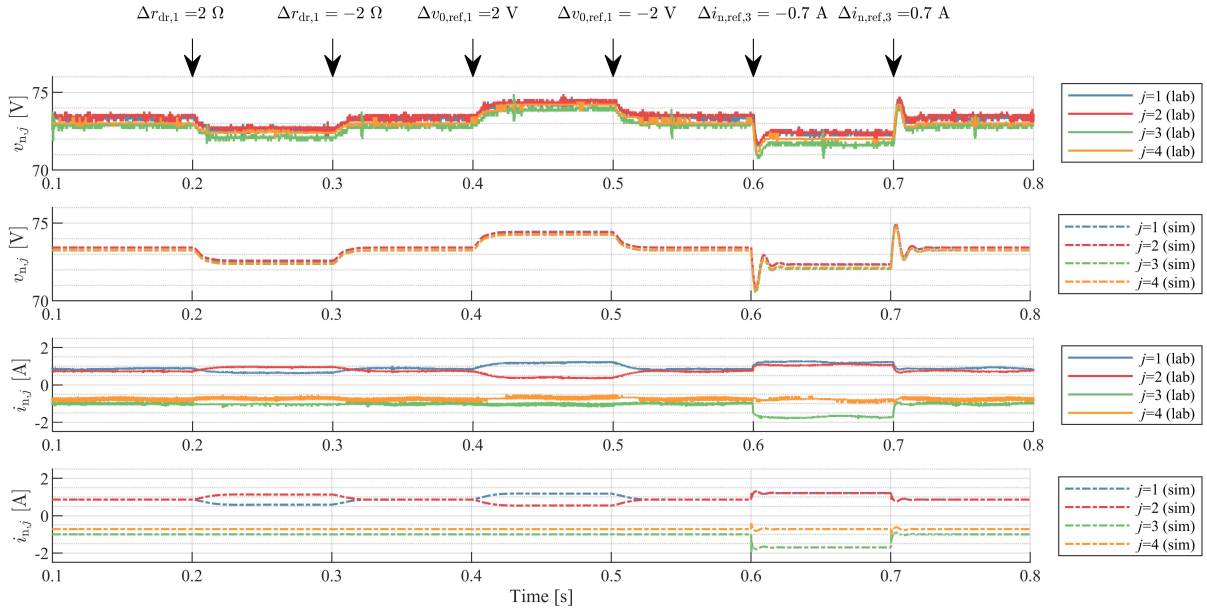


Fig. 10. Laboratory (lab) and simulation (sim) data obtained for $n = 4$ using the topology in Fig. 9, with $I_{n,\text{ref},3} = -1$ A and $I_{n,\text{ref},4} = -0.8$ A, under the application of step changes to $r_{\text{dr},1}$, $v_{0,\text{ref},1}$, and $i_{n,\text{ref},3}$ as indicated by the arrows at the top of the figure; all other parameters are as provided in Table III.

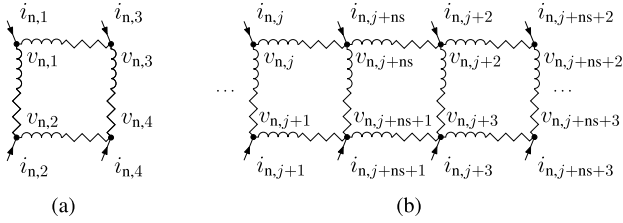


Fig. 11. Topologies for (a) $n = 4$ with $n_s = 2$ and (b) $n \geq 8$ with $2 \cdot n_s = n$.

The first metric β_1 assesses the self-regulatory properties of the state variables and is defined as

$$\beta_1 = \frac{N_{\text{diag,pos}}(\mathbf{A})}{N_{\text{diag}}(\mathbf{A})} \quad (27)$$

where $N_{\text{diag}}(\mathbf{A})$ is the number of diagonal elements $a_{hg} \in \mathbf{A}$, $h = g$; $N_{\text{diag,pos}}(\mathbf{A})$ is the number of positive diagonal elements $a_{hg} > 0$, $h = g$.

The second metric β_2 assesses the interactions between different state variables and is defined as

$$\beta_2 = \frac{N_{\text{link,pos}}(\mathbf{A})}{N_{\text{link}}(\mathbf{A})} \quad (28)$$

where $N_{\text{link}}(\mathbf{A})$ is the number of links of \mathbf{A} . A link is defined as a pair of non-diagonal elements $\{a_{hg} \in \mathbf{A}, a_{gh} \in \mathbf{A}\}$, $h \neq g$. Furthermore, $N_{\text{link,pos}}(\mathbf{A})$ is the number of links for which $a_{hg} \cdot a_{gh} > 0$, $h \neq g$.

The qualitative robustness is assessed for two microgrid sizes, $n = 4$ and $n = 1000$. The results are summarized in Table II and discussed as follows. For both microgrid sizes, none of the diagonal elements are positive, hence $\beta_1 = 0$. This indicates that the state variables are generally self-regulating.

In terms of interactions between the different state variables, there are points of concern due to the presence of positive links and, hence, $\beta_2 > 0$. Further analysis reveals that there is

TABLE II
SUMMARY OF QUALITATIVE ROBUSTNESS ANALYSIS FOR \mathbf{A} OF (3); AS DEFINED IN (27) AND (28), LOW VALUES OF β_1 AND β_2 INDICATE HIGH ROBUSTNESS

n	$N_{\text{diag,pos}}(\mathbf{A})$	β_1	$N_{\text{link,pos}}(\mathbf{A})$	β_2
4	0	0	2	0.00866
1000	0	0	500	0.00003

one positive link for every node in the charging mode. This is the link between the state variable for the ideal capacitor model and one state variable for the input admittance model. The direct connection between the capacitance and the input admittance is also apparent from the small-signal model shown in Fig. 8. The relationship between the capacitance and input admittance is further analyzed in the following quantitative stability analysis, in particular, in the section presenting the two-parameter variation. The number of positive links scales proportionally to n , whereas the total number of links scales proportionally to n^2 . Consequently, and as shown in Table II, the discussed robustness indicator improves with an increase in the size of the microgrid.

B. Analysis of Expandability to $n = 1000$

To assess the expandability of the microgrid, the stability of the swarm microgrid system matrices for different microgrid sizes is analyzed based on their eigenvalues. The system matrix \mathbf{A} in (26) has eigenvalues of $\lambda\{\mathbf{A}\}$, and the system is stable if the real part λ_{re} of eigenvalue λ is negative for all $\lambda\{\mathbf{A}\}$

$$\lambda_{\text{re}}\{\mathbf{A}\} < 0. \quad (29)$$

In addition, the following performance specifications need to be met.

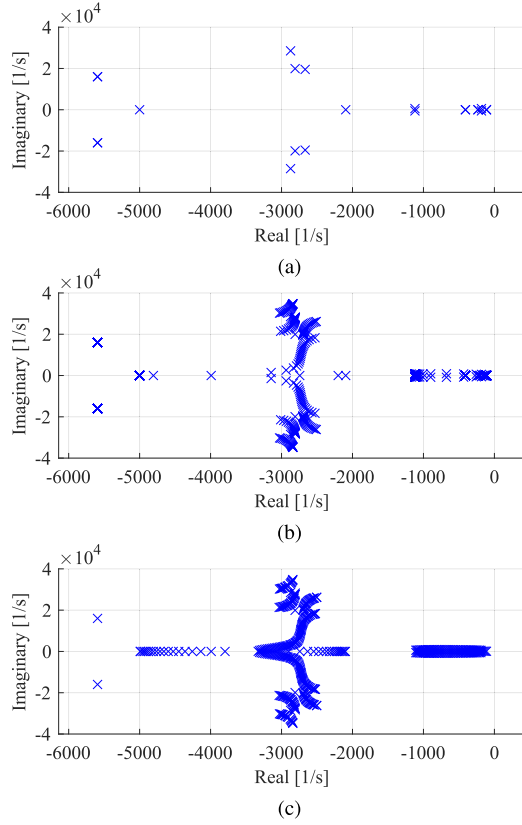


Fig. 12. Eigenvalue plots for swarm microgrids with different numbers of swarm units. (a) $n = 4$. (b) $n = 100$. (c) $n = 1000$. The performance specifications defined in (A.1)–(A.3), (30), and (31) are met for all three assessed cases.

- 1) A nontrivial solution for all steady-state equations can be found. The steady-state equations (A.1)–(A.3) are defined in Appendix B.
- 2) All swarm units in supplying mode must have a positive nodal current

$$I_{n,j} > 0 \quad \forall j = 1, \dots, n_s. \quad (30)$$

- 3) Line losses [53] must be less than 10% of the power drawn by the nodes in the charging mode

$$\frac{\sum_{j=1}^{j=n_s} |P_{n,j}| - \sum_{j=n_s+1}^{j=n} |P_{n,j}|}{\sum_{j=n_s+1}^{j=n} |P_{n,j}|} < 0.1 \quad (31)$$

where $P_{n,j}$ is the nodal power, defined as

$$P_{n,j} = I_{n,j} \cdot V_{n,j}. \quad (32)$$

All three of the abovementioned performance specifications are verified for the following assessments.

The eigenvalues of the system matrix A from (26) derived for $n = 4$, $n = 100$, and $n = 1000$ are presented in Fig. 12(a)–(c), respectively. Due to the increase in system size, the number of eigenvalues also increases. Nevertheless, all eigenvalues have a negative real part. The eigenvalue with the smallest stability margin is the same for all microgrid sizes. Thus, the stability is not affected by the size of the microgrid. Also, the three performance specifications are met for all assessed microgrid sizes. To further examine the ability to expand the microgrid, Section VI-C presents an analysis of the influence of variations in the other microgrid parameters.

C. Robustness Analysis Considering Parameter Variations

In addition to the validation of the effect of the microgrid size on the stability of the system given in Section VI-B, an assessment of the effect of varying all other modeling parameters is presented in this section. The parameter variation ranges are selected by considering a realistic value range for each individual parameter. The size of the microgrid system is kept constant at $n = 1000$. An eigenvalue analysis is conducted to assess the impacts of variations in each parameter on the system stability. The parameters varied include the parameters of the transfer functions modeling the dc–dc converters, as discussed in Section IV. These transfer functions, namely, $Z_o(s)$, $T_{VC}(s)$, $Y_{in}(s)$, and $T_{CC}(s)$, follow the generic structure of (20). The parameter identification for these transfer functions is provided in Appendix C. All parameters of these transfer functions except those identified to have trivial values of $\{1, 0\}$ are considered as part of this analysis. The list of parameters also includes parameters that are less specific to swarm microgrids. For these parameters, value ranges similar to those reported in the literature were chosen [18], [30], [48]. In this section, single-parameter variations are assessed first, followed by an assessment of two-parameter variations.

1) *Single-Parameter Variations*: The single-parameter analysis is summarized in Table III. For each parameter, the symbol, the description, the reference value, the parameter unit, and the parameter variation range from the smallest to the largest value are provided along with the corresponding eigenvalue results. Positive eigenvalues, which indicate an unstable microgrid, are marked in bold font. In addition to the analysis of the eigenvalues, the performance specifications defined in Section VI-B are also assessed for. The subsequent analysis is divided into three parts, discussing the effects of variations in parameters related to the 1) network; 2) supplying mode behavior; and 3) charging mode behavior.

For the network parameters, no single-parameter variation can cause the system to become unstable. In particular, neither the cable length l_c nor the ratio of cable inductance to cable resistance L_c/R_c has a detrimental impact on stability. There is no significant impact on the critical eigenvalues. Considering (24) and the parameter value ranges of the network parameters presented in Table III, the value range for the cable resistance is between $R_c = 2 \text{ m}\Omega$ and $R_c = 2 \text{ }\Omega$. Despite this wide range and the large microgrid size of $n = 1000$, no detrimental impact on stability is found.

Most of the supplying mode parameters do have an impact on the critical eigenvalues, although without making the system unstable. However, variations in the parameters that model the output impedance can result in system instability. The parameters that can lead to an unstable microgrid when varied across their variation ranges are as follows:

- 1) $K_{2,Z}$, the proportional gain of the second-order subsystem of the output impedance.
- 2) ζ_Z , the damping factor of the second-order subsystem of the output impedance.
- 3) $T_{\text{zero},Z}$, the time constant associated with the transfer function zero of the second-order subsystem of the output impedance.

For the charging mode parameters, several single-parameter variations do not have an impact on stability. However, all four parameters concerning the input admittance exert a

TABLE III
PARAMETER DEFINITIONS, VARIATION RANGES, AND EIGENVALUE RESULTS FOR SINGLE-PARAMETER VARIATION
WITH $n = 1000$; NAMING CONVENTIONS ACCORDING TO (20); THE PERFORMANCE SPECIFICATIONS
DEFINED IN (A.1)–(A.3), (30), AND (31) ARE MET FOR ALL ASSESSED VARIATIONS

Symbol	Description	Reference value	Unit	Smallest value	Largest value	Max $\lambda_{re}\{A\}$ [1/s] for smallest value	largest value
Network parameters							
l_c	Length of cable between two swarm units	10.5	m	0.1	100.0	-111	-118
σ_c	Cable conductivity	51.9	$m/(\Omega \cdot mm^2)$	40.0	60.0	-112	-112
A_c	Cable cross-sectional area	2.0	mm^2	1.0	6.0	-112	-111
L_c/R_c	Ratio of cable inductance to cable resistance	0.0002	H/Ω	0.0001	0.0030	-112	-94
Supplying mode parameters							
R_{dr}	Steady-state droop resistance	3.00	Ω	0.01	15.00	-6	-153
$V_{0,ref}$	Steady-state reference zero-current voltage	76.0	V	60.0	120.0	-112	-112
$T_{L,PF}$	Low-pass filter time constant, where $f_{L,PF} = 1/T_{L,PF}$	0.0050	s	0.0001	0.0500	-96	-14
$T_{1,VC}$	Time constant associated with the pole of the first-order subsystem of $T_{VC}(s)$	0.0025	s	0.0010	0.1000	-126	-7
$T_{2,Z}$	Time constant associated with the double pole pair of the second-order system of $Z_o(s)$	0.0018	s	0.0010	0.0025	-12	-127
$K_{2,Z}$	Proportional gain of the second-order subsystem of $Z_o(s)$	0.10	V/A	-0.15	0.15	34 025	-108
ζ_Z	Damping factor of the second-order subsystem of $Z_o(s)$	0.99	[-]	0.20	0.99	46	-112
$T_{zero,Z}$	Time constant associated with the transfer function zero of the second-order subsystem of $Z_o(s)$	0.3	s	-0.1	0.5	14 451	-91
Charging mode parameters							
$I_{n,ref}$	Steady-state nodal current reference	-1.0	A	-0.1	-10.0	-112	-112
C	Input capacitance of a step-down converter	0.000142	F	0.000014	0.000500	-112	-112
$T_{2,CC}$	Time constant associated with the double pole pair of the second-order system of $T_{CC}(s)$	0.000059	s	0.000010	0.001000	-112	-112
ζ_{CC}	Damping factor of the second-order subsystem of $T_{CC}(s)$	0.3	[-]	0.1	1.0	-112	-112
$K_{2,Y}$	Proportional gain of the second-order subsystem of $Y_{in}(s)$	0.0010	A/V	0.0005	0.0020	-112	20
$T_{2,Y}$	Time constant associated with the double pole pair of the second-order system of $Y_{in}(s)$	0.00080	s	0.00001	0.00100	14 775	-112
ζ_Y	Damping factor of the second-order subsystem of $Y_{in}(s)$	0.90	[-]	0.10	0.99	141	-112
$T_{zero,Y}$	Time constant associated with the transfer function zero of the second-order subsystem of $Y_{in}(s)$	-0.16	s	-0.50	0.10	198	-112

strong detrimental impact on stability. These parameters are as follows:

- 1) $K_{2,Y}$, the proportional gain of the second-order subsystem of the input admittance.
- 2) $T_{2,Y}$, the time constant associated with the double pole pair of the second-order system of the input admittance.
- 3) ζ_Y , the damping factor of the second-order subsystem of the input admittance.
- 4) $T_{zero,Y}$, the time constant associated with the transfer function zero of the second-order subsystem of the input admittance.

The identified parameters that can cause unstable microgrid configurations due to single-parameter variations form the set $\mathbb{K}_{unstable}$

$$\mathbb{K}_{unstable} = \{K_{2,Z}, \zeta_Z, T_{zero,Z}, K_{2,Y}, T_{2,Y}, \zeta_Y, T_{zero,Y}\}. \quad (33)$$

This set is further analyzed in Section VI-C2, focusing on two-parameter variations.

2) *Two-Parameter Variations*: A more in-depth analysis is undertaken by assessing two-parameter variations. The results are summarized in Table IV and discussed as follows. For each considered two-parameter variation, the first parameter is one of the seven parameters from the set $\mathbb{K}_{unstable}$, defined in (33). The second parameter is one of the 20 parameters defined in Table III. Both parameters are varied over the ranges specified in Table III with N_{var} different values. With $N_{var} = 10$, for each two-parameter variation combination,

the total number of microgrid configurations assessed is $N_{var}^2 = 100$. Accordingly, the number of microgrid system matrices assessed in this analysis totals $7 \cdot 20 \cdot 100 = 14\,000$. Due to the high computational effort associated with such a large number of microgrid simulations, the system size is reduced to $n = 100$. The reference eigenvalue plot for $n = 100$ is provided in Fig. 12(b).

To quantify the impact of each two-parameter variation, the percentage of corresponding microgrid configurations that are unstable is assessed. The two-parameter variation results are compared against a baseline. This baseline is defined as the percentage of unstable microgrids under the single-parameter variation of only the first parameter, a member of $\mathbb{K}_{unstable}$.

The baseline analysis is undertaken first. As shown in Table IV, among all parameters in $\mathbb{K}_{unstable}$, $K_{2,Z}$ is associated with the highest percentage of unstable microgrid configurations: 50% of the associated microgrid configurations are unstable. For the other parameters in $\mathbb{K}_{unstable}$, the percentage of unstable microgrid configurations under single-parameter variations is between 10% and 30%.

The results for the two-parameter variations are provided in Table IV and are discussed as follows, starting with the network parameters, followed by the supplying mode parameters, and concluding with the charging mode parameters. The network parameters do not have a significant impact on the percentage of unstable microgrid configurations in comparison with the baseline. For example, for the baseline of

TABLE IV

RESULTS OF TWO-PARAMETER VARIATIONS WITH $n = 100$; PARAMETER DEFINITIONS AND VARIATION RANGES CONSISTENT WITH TABLE III; THE PERFORMANCE SPECIFICATIONS DEFINED IN (A.1)–(A.3), (30), AND (31) ARE MET FOR ALL ASSESSED VARIATIONS

First parameter	$K_{2,Z}$	ζ_Z	$T_{zero,Z}$	$K_{2,Y}$	$T_{2,Y}$	ζ_Y	$T_{zero,Y}$
Second parameter	Percentage of microgrid configurations that are unstable						
Baseline, single-parameter variations							
—	50%	20%	20%	10%	10%	20%	30%
Network parameters, two-parameter variations							
l_c	50%	23%	20%	18%	16%	25%	38%
σ_c	50%	20%	20%	10%	10%	20%	31%
A_c	50%	20%	20%	10%	10%	20%	32%
L_c/R_c	50%	20%	20%	14%	37%	37%	36%
Supplying mode parameters, two-parameter variations							
R_{dr}	50%	21%	20%	6%	10%	20%	32%
$V_{0,ref}$	50%	20%	20%	10%	10%	20%	30%
T_{LFP}	50%	21%	20%	17%	10%	20%	39%
$T_{1,YC}$	50%	27%	20%	19%	10%	20%	39%
$T_{2,Z}$	53%	34%	25%	21%	10%	31%	34%
$K_{2,Z}$	—	59%	50%	56%	55%	58%	61%
ζ_Z	—	—	37%	44%	23%	43%	48%
$T_{zero,Z}$	—	—	—	32%	28%	35%	40%
Charging mode parameters, two-parameter variations							
$I_{n,ref}$	50%	20%	20%	10%	10%	20%	30%
C	51%	16%	22%	10%	10%	19%	22%
$T_{2,CC}$	50%	20%	20%	10%	10%	20%	30%
ζ_{CC}	50%	20%	20%	10%	10%	20%	30%
$K_{2,Y}$	—	—	—	—	27%	42%	38%
$T_{2,Y}$	—	—	—	—	—	32%	41%
ζ_Y	—	—	—	—	—	—	47%
$T_{zero,Y}$	—	—	—	—	—	—	—

the single-parameter variation of ζ_Z , 20% of the microgrid configurations are unstable. In comparison, for the two-parameter variation of l_c and ζ_Z , 23% of the microgrid configurations are unstable. The only parameter that has a significant impact on stability when varied together with another parameter is the ratio L_c/R_c when varied together with $T_{2,Y}$. Here, the percentage of unstable microgrid configurations is 3.7 times greater than that of the baseline. Such strong impact can be explained by the resonance of the line inductance with the input admittance. This is one reason why nodal CC is an important part of the control strategy summarized in Table I.

The supplying mode parameters give rise to one two-parameter variation that leads to a reduction in the percentage of unstable microgrid configurations: the two-parameter variation of R_{dr} and $K_{2,Y}$. This relationship is shown in more detail in Fig. 13, where all $N_{var}^2 = 100$ microgrid configurations associated with this two-parameter variation are represented. Unstable microgrid configurations are marked with red crosses, and stable microgrid configurations are marked with blue circles. For better orientation, the reference parameter set from Table III is also indicated. The results in Fig. 13 show that a wide range of values for R_{dr} is allowed even for extreme values of $K_{2,Y}$. An important enabler for this wide allowed range of R_{dr} is the LPF, which enables a damped implementation of the droop equation (1). This relationship is demonstrated when undertaking the same analysis of varying R_{dr} and $K_{2,Y}$ but with a much higher value for f_{LFP} , as presented in Fig. 14. The high value of f_{LFP} means that the LPF is effectively deactivated. The results provided in Fig. 14 show

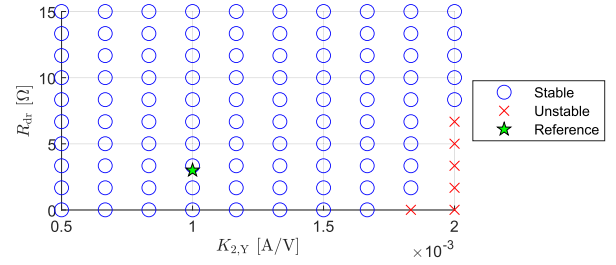


Fig. 13. Stability analysis for two-parameter variation of R_{dr} and $K_{2,Y}$ with $f_{LFP} = 200$ Hz, showing that 6% of the microgrid configurations are unstable; the individual parameter definitions, reference values, and variation ranges are consistent with Table III.

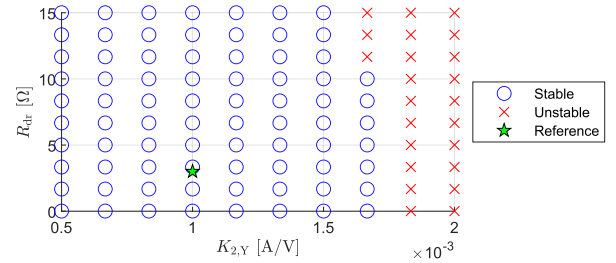


Fig. 14. Stability analysis for two-parameter variation of R_{dr} and $K_{2,Y}$ with $f_{LFP} = 10$ kHz, showing that 23% of the microgrid configurations are unstable; the individual parameter definitions, reference values, and variation ranges are consistent with Table III.

that when the LPF is deactivated, the range of values for R_{dr} that result in a stable microgrid configuration is much more limited.

Supplying mode parameters other than R_{dr} have a detrimental impact on stability. The most severe impact is exerted by the parameters related to the output impedance. When any two of the four parameters modeling the output impedance are varied simultaneously, the number of unstable microgrid configurations increases significantly in comparison with the baseline. However, an even stronger increase in the number of unstable microgrid configurations is observed when an output impedance parameter is varied together with an input admittance parameter. The strongest impact is observed when varying $K_{2,Z}$ and $K_{2,Y}$ together. This two-parameter variation of $K_{2,Z}$ and $K_{2,Y}$ is shown in Fig. 15. To attain a stable microgrid configuration, the value of $K_{2,Z}$ needs to be positive, and $K_{2,Y}$ should be small. As long as the values are close to the reference values, the microgrid configurations are stable.

For the charging mode parameters, the results show a similar pattern. The two-parameter sets that include two input admittance values lead to an increase in the number of unstable microgrids. However, the variation of the input capacitance C has a beneficial effect. For example, when $T_{zero,Y}$ is varied together with C , the percentage of unstable microgrids decreases from 30% to 22%. This direct link between the model of the input capacitor and the model of the input admittance was already identified in Section VI-A during the qualitative assessment. Also for ζ_Z , the variation of C has a positive impact. The two-parameter variation of C and ζ_Z is shown in Fig. 16. A large value of C helps to attain stable microgrid configurations, even for low values of ζ_Z .

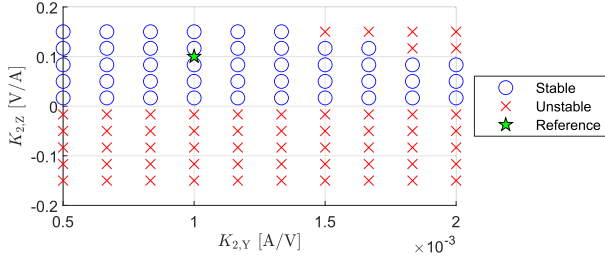


Fig. 15. Stability analysis for two-parameter variation of $K_{2,Z}$ and $K_{2,Y}$, showing that 56% of the microgrid configurations are unstable; the individual parameter definitions, reference values, and variation ranges are consistent with Table III.

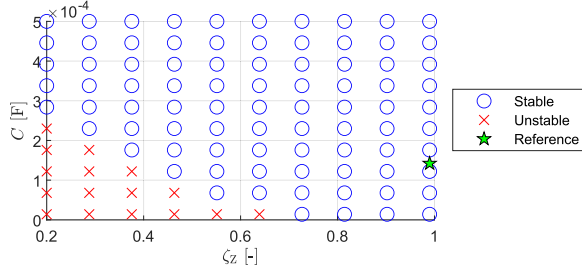


Fig. 16. Stability analysis for two-parameter variation of C and ζ_Z , showing that 16% of the microgrid configurations are unstable; the individual parameter definitions, reference values, and variation ranges are consistent with Table III.

Because both the input admittance and the output impedance have a strong impact on microgrid stability, a more compact way of representing two-parameter variation results is provided in Fig. 17. Here, the step response behaviors of the battery-connected converters of the individual swarm units when disconnected from the microgrid are categorized into allowed areas and no-go areas. Allowed areas, which are shaded in light gray, represent the step responses of parameter value sets that are required to attain a stable microgrid configuration. No-go areas, which are shaded in dark gray, represent the step responses of parameter value sets that result in an unstable microgrid configuration.

In Fig. 17(a), the characterization of the output impedance based on the response to a change in $\tilde{i}_{n,j}$ is shown. Allowed and no-go behavior areas are defined. Specific examples are shown for the variation pair of $T_{2,Z}$ and $T_{zero,Z}$. The input admittance is characterized in the same manner in Fig. 17(b) based on the response to a change in $\tilde{v}_{n,j}$. Allowed and no-go behavior areas are defined, and specific examples are shown for the variation pair of $T_{2,Y}$ and $T_{zero,Y}$.

The representation in terms of allowed and no-go areas is intended to provide a concise tool for practical implementation. In particular, these definitions enable rapid assessment of individual converters in terms of their suitability for a swarm microgrid implementation. Such assessment must be carried out with the converter connected to a battery, as shown in Fig. 6.

D. Summary of Key Results

This section summarizes the key results, synthesizing the practical value of this work. Section VI-B demonstrated the expandability of a swarm microgrid to a large size of up to 1000 swarm units. Section VI-C1 established the low sensitivity of this stability to changes in the model parameters. In Section VI-C2, this robustness was assessed further, leading to the definition of allowed and no-go areas for

converter behavior. It is important to emphasize that all of these assessments were possible without knowledge of the internal structures of the converters. This is particularly relevant for organizations implementing swarm microgrids. Such an organization will most likely not have access to the details of the internal structures of the power converters.

The following summary aims to enable such organizations to ensure stable swarm microgrid operation with only a black-box behavioral assessment using standard laboratory equipment. The criteria listed in the following can be utilized early on in a swarm microgrid project, particularly during planning and procurement activities.

- 1) All swarm units include a battery, as shown in Fig. 2. This is essential for the following statements, in particular, for the converter behavior analysis. Details of the converter behavior models are shown in Fig. 6.
- 2) The control strategy summarized in Table I is to be followed. For units operating in the supplying mode, this includes the reference parameters to enable droop control as per (1) and an LPF for this droop control scheme. For units operating in the charging mode, this includes the nodal CC scheme. An overview of all input and output parameters is provided in Fig. 4.
- 3) The network parameters have no significant influence on stability, as shown in Table III. Neither a variation of the line inductance nor a variation of parameters determining the line resistance leads to an unstable system. The relevant sizing and topological layout should be determined using other methods, such as power flow optimization.
- 4) For supplying mode operation using step-up conversion, the converter must inherently provide output VC. Furthermore, the output impedance behavior of the step-up converter is critical to swarm microgrid stability. A step response characterization of the output impedance must fall within the allowed area shaded in light gray in Fig. 17(a).
- 5) For charging mode operation using step-down conversion, the converter must inherently provide input CC. Furthermore, the input admittance behavior of the step-down converter is critical to swarm microgrid stability. A step response characterization of the input admittance must fall within the allowed area shaded in light gray in Fig. 17(b).

All of the presented validations are to be undertaken with batteries connected to the converters. These batteries should be of a type and condition as similar as possible to those to be used in field deployment.

VII. CONCLUSION

The concept of swarm electrification is based on modular, rapidly deployable, and expandable swarm microgrids. In this article, a decentralized control strategy that enables self-stabilization for swarm electrification, even under changing topological conditions, was developed and analyzed. To validate the performance of the proposed control strategy, a mathematical model of swarm microgrids of various sizes was developed. This model captures the core architectural attributes of swarm microgrids. To achieve a realistic but highly scalable model, a cascaded system modeling approach

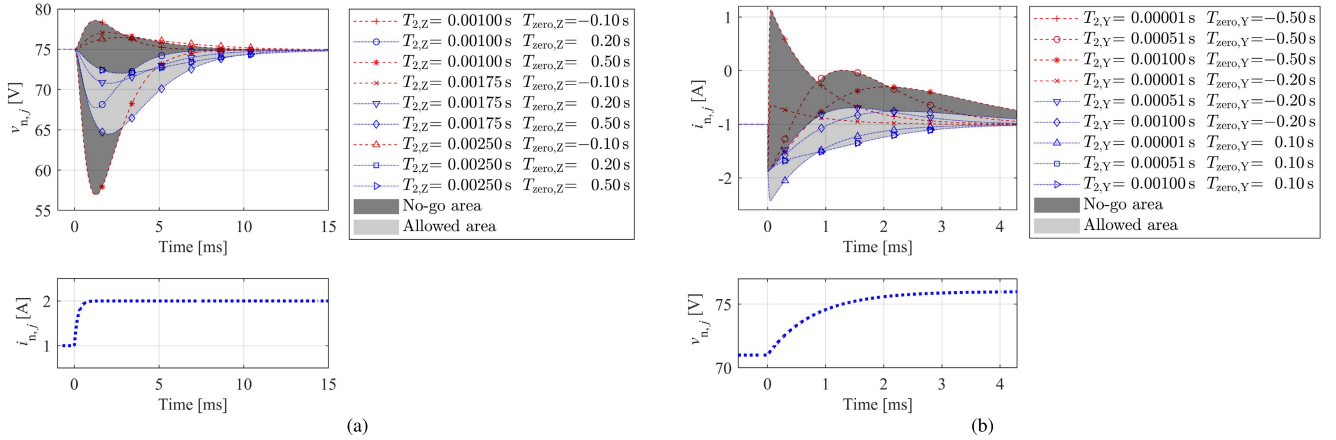


Fig. 17. Step-response behavior categorized into allowed areas (light gray) and no-go areas (dark gray) in terms of microgrid stability. (a) Output impedance step responses of battery-supplied step-up converter. (b) Input admittance step responses of battery-charging step-down converter. The examples of parameter value sets describing behavior that results in an unstable microgrid configuration are marked by dashed red lines, and the examples of parameter value sets describing behavior that results in a stable microgrid configuration are marked by solid blue lines.

was adopted in the model development process while integrating the gray-box modeling of individual power electronic converters. Such a swarm microgrid was demonstrated to be stable and robust on the basis of experimental validation using dual-active-bridge converters, eigenvalue analysis, and an assessment of the influence of parameter variations. The model for large-scale deployment demonstrated a high stability margin, even for large swarm microgrids of up to 1000 swarm units. The unique *ad hoc* deployability of swarm microgrids makes them highly valuable for applications in energy access and emergency relief situations.

APPENDIX

A. Application of Swarm Microgrids

Swarm microgrids that interconnect SHSs are deployed across Bangladesh [54]. An example of swarm microgrid components in operation is provided in Fig. 18. This figure shows a tea stall that has an SHS and is connected to a swarm microgrid. The SHS, cable connection to neighboring buildings, and a telecommunication tower are marked. The swarm microgrid is located in the Faridpur District, in the south of Bangladesh.

B. Steady-State Equations

The analysis is undertaken around a steady-state operating point. The steady-state values are obtained via a dc circuit analysis. The following convention is used: $x = X + \tilde{x}$, where X is the steady-state value, and \tilde{x} is the small-signal perturbation.

For swarm units operating in the supplying mode, the node voltages must satisfy the droop equation (1) for the steady-state values as well

$$V_{n,j} = V_{0,ref,j} - R_{dr,j} \cdot I_{n,j} \quad \forall j = 1, \dots, n_s. \quad (\text{A.1})$$

For swarm units operating in the charging mode, the nodal currents are directly controlled, as specified in Table I. Therefore, the steady-state currents match the desired reference currents as follows:

$$I_{n,j} = I_{n,ref,j} \quad \forall j = n_s + 1, \dots, n. \quad (\text{A.2})$$



Fig. 18. Swarm microgrid components in operation: (a) SHS installed at a tea stall. (b) swarm microgrid cable connection to neighboring buildings. (c) Telecommunication tower for data connectivity.

In addition, Ohm's law must be satisfied for all cables, as shown in Fig. 5 and defined in (23)

$$\Delta V_{c,k} = R_c \cdot I_{c,k} \quad \forall k = 1, \dots, m. \quad (\text{A.3})$$

C. Gray-Box Model Identification

The gray-box model behaviors for both converter topologies derived in Section IV-C are identified on the basis of input–output step responses, as suggested in [35]. The identification follows the generic LTI function defined in (20). The identified parameter values are provided in the third column of Table III.

Laboratory experiments were performed using lead-acid batteries and dual-active-bridge converters that functioned as both step-up and step-down converters. The dual-active-bridge converters were digitally controlled. The digital controller used was a low-cost 32-bit microcontroller unit. Measurements were sampled at 100 kHz; control outputs were updated at 10 kHz.

A KIKUSUI-PLZ-1004W electronic load was used to produce transient inputs. Data collection was undertaken using 50-MHz scopes of type GW-INSTEK GDS-1054B

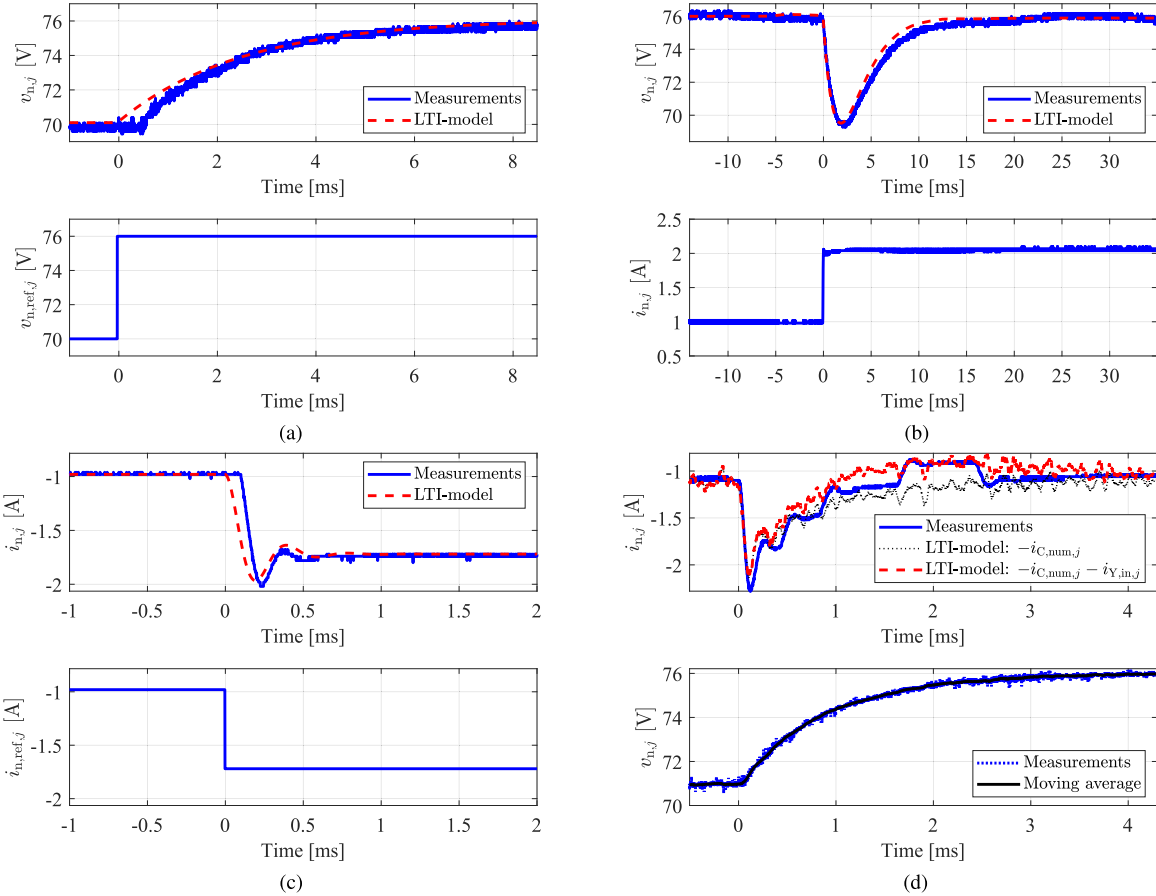


Fig. 19. Parameter identification for the transfer functions of the gray-box converter models. (a) $T_{VC}(s)$. (b) $Z_o(s)$. (c) $T_{CC}(s)$. (d) $Y_{in}(s)$.

with B&K Precision model CP62 current probes and Testec TT-SI 9002 differential voltage probes.

1) *Supplying Mode VC*: The VC behavior was identified based on the response to a change in $\tilde{v}_{n,ref,j}$, as shown in Fig. 19(a). The transfer function was identified as a first-order system, with $K_{1,VC} = 1$ and $K_{2,VC} = 0$, as follows:

$$T_{VC}(s) = \frac{1}{1 + T_{1,VC} \cdot s}. \quad (A.4)$$

2) *Supplying Mode Output Impedance*: The output impedance behavior was analyzed based on an increase in $\tilde{i}_{n,j}$, as shown in Fig. 19(b). The output impedance was identified as a second-order system with $K_{1,Z} = 0$

$$Z_o(s) = \frac{K_{2,Z} \cdot (1 + T_{zero,Z} \cdot s)}{1 + 2 \cdot \zeta_Z \cdot T_{2,Z} \cdot s + (T_{2,Z} \cdot s)^2}. \quad (A.5)$$

3) *Charging Mode CC*: The behavior of the input CC loop was analyzed for a stepwise change in $\tilde{i}_{n,ref,j}$, as shown in Fig. 19(c). The transfer function was identified as a second-order system, with $K_{1,CC} = 0$, $K_{2,CC} = 1$, and $T_{zero,CC} = 0$, as follows:

$$T_{CC}(s) = \frac{1}{1 + 2 \cdot \zeta_{CC} \cdot T_{2,CC} \cdot s + (T_{2,CC} \cdot s)^2}. \quad (A.6)$$

4) *Charging Mode Input Admittance*: To obtain $Y_{in}(s)$, the reference nodal current must be held constant; therefore, $\tilde{i}_{CC} = 0$. Furthermore, the reciprocal effects between the input admittance and the capacitor must be accounted for, as shown

in Fig. 6(d). The step response to a change in the input voltage can be used to identify the parameters of $Y_{in}(s)$ as long as the behavior of the capacitor is accounted for. The capacitor was modeled as having ideal behavior according to (14). To assess the measured step response data, a numerical approximation of such an ideal capacitor, $\tilde{i}_{C,num,j}$, was used

$$\tilde{i}_{C,num,j} = C \cdot \frac{\Delta \tilde{v}_{n,j}}{\Delta t}. \quad (A.7)$$

With this approximation, (16) can be written as

$$\tilde{i}_{n,j} \Big|_{\tilde{i}_{CC}=0} = -\tilde{i}_{C,num,j} - \tilde{i}_{Y,in,j}. \quad (A.8)$$

The following detailed analysis process was followed.

- 1) The step-down converter was perturbed through a change in $\tilde{v}_{n,j}$. The sampling time for the measurement was $1 \mu\text{s}$.
- 2) Then, $\tilde{i}_{C,num,j}$ was computed according to (A.7).
- 3) As the derivative approximation in (A.7) is susceptible to noise, the data needed to be filtered. For both the measured quantity $\tilde{v}_{n,j}$ and the calculated quantity $\tilde{i}_{C,num,j}$, a $50\text{-}\mu\text{s}$ moving average filter was applied.
- 4) Then, the parameters of $\tilde{i}_{Y,in,j}$ were identified according to (A.8).

As shown in Fig. 19(d), the dotted black curve corresponding to the capacitor model adequately simulates the response in the time range from 0 ms to approximately 0.5 ms after the voltage change. However, after 0.5 ms, the curves deviate. Therefore, the admittance needs to model this particular

behavior, with a substantial deviation from the steady-state value at 2 ms and a return close to the initial steady-state value at approximately 4 ms. Accordingly, the transfer function for the admittance $Y_{in}(s)$ was identified as a second-order system with $K_{1,Y} = 0$

$$Y_{in}(s) = \frac{K_{2,Y} \cdot (1 + T_{zero,Y} \cdot s)}{1 + 2 \cdot \zeta_Y \cdot T_{2,Y} \cdot s + (T_{2,Y} \cdot s)^2}. \quad (A.9)$$

ACKNOWLEDGMENT

The authors would like to thank the ME SOLshare Laboratory Team, Dhaka, Bangladesh, particularly, Md. Aminul Islam, for supporting the laboratory measurements presented in this work.

REFERENCES

- [1] IEA, IRENA, UNSD, WB, and WHO, "Tracking SDG 7: The energy progress report," World Bank, Washington, DC, USA, Tech. Rep. 4, 2019.
- [2] H. Kirchhoff and K. Strunz, "Key drivers for successful development of peer-to-peer microgrids for swarm electrification," *Appl. Energy*, vol. 244, pp. 46–62, Jun. 2019.
- [3] S. Groh, D. Philipp, B. E. Lasch, and H. Kirchhoff, "Swarm electrification: Investigating a paradigm shift through the building of microgrids bottom-up," in *Decentralized Solutions for Developing Economies: Addressing Energy Poverty Through Innovation* (Springer Proceedings in Energy), S. Groh, J. van der Straeten, B. E. Lasch, D. Gershenson, W. L. Filho, and D. M. Kammen, Eds. Cham, Switzerland: Springer, 2015, pp. 3–22.
- [4] T. S. Ustun, S. M. S. Hussain, H. Kirchhoff, B. Ghaddar, K. Strunz, and I. Lestas, "Data standardization for smart infrastructure in first-access electricity systems," *Proc. IEEE*, vol. 107, no. 9, pp. 1790–1802, Sep. 2019.
- [5] SREDA. (Aug. 2021). *Technology Wise RE Generation Statistics*. [Online]. Available: <http://www.renewableenergy.gov.bd/>
- [6] UNDESA. (Nov. 2017). *UN Awards U.S. \$1 Million for Bangladesh Solar Entrepreneurship Initiative to Aid Rural Electrification—United Nations Department of Economic and Social Affairs*. [Online]. Available: <https://www.un.org/>
- [7] P. Fairley, "'Swarm electrification' powers villages—ME SOLshare links isolated PV systems," *IEEE Spectr.*, vol. 55, no. 4, p. 21, Apr. 2018.
- [8] A. Riccobono and E. Santi, "Comprehensive review of stability criteria for DC power distribution systems," *IEEE Trans. Ind. Appl.*, vol. 50, no. 5, pp. 3525–3535, Sep. 2014.
- [9] M. Adly and K. Strunz, "DC microgrid small-signal stability and control: Sufficient stability criterion and stabilizer design," *Sustain. Energy, Grids Neww.*, vol. 26, Jun. 2021, Art. no. 100435.
- [10] M. Saleh, Y. Esa, and A. A. Mohamed, "Communication-based control for DC microgrids," *IEEE Trans. Smart Grid*, vol. 10, no. 2, pp. 2180–2195, Mar. 2019.
- [11] A. Werth *et al.*, "Peer-to-peer control system for DC microgrids," *IEEE Trans. Smart Grid*, vol. 9, no. 4, pp. 3667–3675, Jul. 2018.
- [12] T. Dragičević, X. Lu, J. C. Vasquez, and J. M. Guerrero, "DC microgrids—Part I: A review of control strategies and stabilization techniques," *IEEE Trans. Power Electron.*, vol. 31, no. 7, pp. 4876–4891, Jul. 2016.
- [13] E. Espina, J. Llanos, C. Burgos-Mellado, R. Cárdenas-Dobson, M. Martínez-Gómez, and D. Sáez, "Distributed control strategies for microgrids: An overview," *IEEE Access*, vol. 8, pp. 193412–193448, 2020.
- [14] X. Lu, K. Sun, J. M. Guerrero, J. C. Vasquez, L. Huang, and J. Wang, "Stability enhancement based on virtual impedance for DC microgrids with constant power loads," *IEEE Trans. Smart Grid*, vol. 6, no. 6, pp. 2770–2783, Nov. 2015.
- [15] S. Anand and B. G. Fernandes, "Reduced-order model and stability analysis of low-voltage DC microgrid," *IEEE Trans. Ind. Electron.*, vol. 60, no. 11, pp. 5040–5049, Nov. 2013.
- [16] X. Zhang, X. Ruan, and Q.-C. Zhong, "Improving the stability of cascaded DC/DC converter systems via shaping the input impedance of the load converter with a parallel or series virtual impedance," *IEEE Trans. Ind. Electron.*, vol. 62, no. 12, pp. 7499–7512, Dec. 2015.
- [17] Q. Xu, N. Vafamand, L. Chen, T. Dragičević, L. Xie, and F. Blaabjerg, "Review on advanced control technologies for bidirectional DC/DC converters in DC microgrids," *IEEE J. Emerg. Sel. Topics Power Electron.*, vol. 9, no. 2, pp. 1205–1221, Apr. 2021.
- [18] M. Hamzeh, M. Ghafouri, H. Karimi, K. Sheshyekani, and J. M. Guerrero, "Power oscillations damping in DC microgrids," *IEEE Trans. Energy Convers.*, vol. 31, no. 3, pp. 970–980, Sep. 2016.
- [19] Q. Xu *et al.*, "A decentralized dynamic power sharing strategy for hybrid energy storage system in autonomous DC microgrid," *IEEE Trans. Ind. Electron.*, vol. 64, no. 7, pp. 5930–5941, Jul. 2017.
- [20] S. K. Kollimalla, M. K. Mishra, A. Ukil, and H. B. Gooi, "DC grid voltage regulation using new HESS control strategy," *IEEE Trans. Sustain. Energy*, vol. 8, no. 2, pp. 772–781, Apr. 2017.
- [21] M. Farrokhhabadi, S. König, C. A. Cañizares, K. Bhattacharya, and T. Leibfried, "Battery energy storage system models for microgrid stability analysis and dynamic simulation," *IEEE Trans. Power Syst.*, vol. 33, no. 2, pp. 2301–2312, Mar. 2018.
- [22] N. L. Diaz, T. Dragičević, J. C. Vasquez, and J. M. Guerrero, "Intelligent distributed generation and storage units for DC microgrids—A new concept on cooperative control without communications beyond droop control," *IEEE Trans. Smart Grid*, vol. 5, no. 5, pp. 2476–2485, Sep. 2014.
- [23] M. Kim and A. Kwasinski, "Decentralized hierarchical control of active power distribution nodes," *IEEE Trans. Energy Convers.*, vol. 29, no. 4, pp. 934–943, Dec. 2014.
- [24] K. Strunz, E. Abbasi, and D. N. Huu, "DC microgrid for wind and solar power integration," *IEEE J. Emerg. Sel. Topics Power Electron.*, vol. 2, no. 1, pp. 115–126, Mar. 2014.
- [25] M. S. Sadabadi, Q. Shafiee, and A. Karimi, "Plug-and-play robust voltage control of DC microgrids," *IEEE Trans. Smart Grid*, vol. 9, no. 6, pp. 6886–6896, Nov. 2018.
- [26] M. Nasir, Z. Jin, H. A. Khan, N. A. Zaffar, J. C. Vasquez, and J. M. Guerrero, "A decentralized control architecture applied to DC nanogrid clusters for rural electrification in developing regions," *IEEE Trans. Power Electron.*, vol. 34, no. 2, pp. 1773–1785, Feb. 2019.
- [27] Y. Gui, R. Han, J. M. Guerrero, J. C. Vasquez, B. Wei, and W. Kim, "Large-signal stability improvement of DC–DC converters in DC microgrid," *IEEE Trans. Energy Convers.*, vol. 36, no. 3, pp. 2534–2544, Sep. 2021.
- [28] W. Xie, M. Han, W. Cao, J. M. Guerrero, and J. C. Vasquez, "System-level large-signal stability analysis of droop-controlled DC microgrids," *IEEE Trans. Power Electron.*, vol. 36, no. 4, pp. 4224–4236, Apr. 2021.
- [29] M. Tabari and A. Yazdani, "A mathematical model for stability analysis of a DC distribution system for power system integration of plug-in electric vehicles," *IEEE Trans. Veh. Technol.*, vol. 64, no. 5, pp. 1729–1738, May 2015.
- [30] T. L. Nguyen, J. M. Guerrero, and G. Griepentrog, "A self-sustained and flexible control strategy for islanded DC nanogrids without communication links," *IEEE J. Emerg. Sel. Topics Power Electron.*, vol. 8, no. 1, pp. 877–892, Mar. 2020.
- [31] P. A. Madduri, J. Poon, J. Rosa, M. Podolsky, E. A. Brewer, and S. R. Sanders, "Scalable DC microgrids for rural electrification in emerging regions," *IEEE J. Emerg. Sel. Topics Power Electron.*, vol. 4, no. 4, pp. 1195–1205, Dec. 2016.
- [32] S. Chevalier, F. M. Ibanez, K. Cavanagh, K. Turitsyn, L. Daniel, and P. Vorobei, "Network topology invariant stability certificates for DC microgrids with arbitrary load dynamics," *IEEE Trans. Power Syst.*, vol. 37, no. 3, pp. 1782–1797, May 2022.
- [33] H. Qin and J. W. Kimball, "Generalized average modeling of dual active bridge DC–DC converter," *IEEE Trans. Power Electron.*, vol. 27, no. 4, pp. 2078–2084, Apr. 2012.
- [34] V. Valdivia, A. Barrado, A. Lázaro, M. Sanz, D. L. del Moral, and C. Raga, "Black-box behavioral modeling and identification of DC–DC converters with input current control for fuel cell power conditioning," *IEEE Trans. Ind. Electron.*, vol. 61, no. 4, pp. 1891–1903, Apr. 2014.
- [35] V. Valdivia, A. Barrado, A. Lázaro, P. Zumel, C. Raga, and C. Fernández, "Simple modeling and identification procedures for 'black-box' behavioral modeling of power converters based on transient response analysis," *IEEE Trans. Power Electron.*, vol. 24, no. 12, pp. 2776–2790, Dec. 2009.
- [36] C. Fernández *et al.*, "Simple model and experimental identification of a fuel-cell-based power supply oriented to system-level analysis," *IEEE Trans. Power Electron.*, vol. 26, no. 7, pp. 1868–1878, Jul. 2011.
- [37] I. Cvetkovic, D. Boroyevich, P. Mattavelli, F. C. Lee, and D. Dong, "Unterminated small-signal behavioral model of DC–DC converters," *IEEE Trans. Power Electron.*, vol. 28, no. 4, pp. 1870–1879, Apr. 2013.

- [38] J. Siegers, S. Arrua, and E. Santi, "Stabilizing controller design for multibus MVdc distribution systems using a passivity-based stability criterion and positive feedforward control," *IEEE J. Emerg. Sel. Topics Power Electron.*, vol. 5, no. 1, pp. 14–27, Mar. 2017.
- [39] A. Francés, R. Asensi, and J. Uceda, "Blackbox polytopic model with dynamic weighting functions for DC–DC converters," *IEEE Access*, vol. 7, pp. 160263–160273, 2019.
- [40] U. Orji *et al.*, "Adaptive zonal protection for ring microgrids," *IEEE Trans. Smart Grid*, vol. 8, no. 4, pp. 1843–1851, Jul. 2017.
- [41] B. Heinbokel, H. Kirchhoff, T. Dragičević, and J. M. Guerrero, "Zonal protection of DC swarm microgrids using a novel multi-terminal grid interface with decentralized control," in *Proc. 50th Int. Univ. Power Eng. Conf. (UPEC)*, Stoke on Trent, U.K., Jan. 2015, pp. 1–6.
- [42] H. Hajebrahimim, S. M. Kaviri, S. Eren, and A. Bakhshai, "A new energy management control method for energy storage systems in microgrids," *IEEE Trans. Power Electron.*, vol. 35, no. 11, pp. 11612–11624, Mar. 2020.
- [43] J.-O. Lee, Y.-S. Kim, T.-H. Kim, and S.-I. Moon, "Novel droop control of battery energy storage systems based on battery degradation cost in islanded DC microgrids," *IEEE Access*, vol. 8, pp. 119337–119345, 2020.
- [44] G. Liu, P. Mattavelli, and S. Saggini, "Resistive–capacitive output impedance shaping for droop-controlled converters in DC microgrids with reduced output capacitance," *IEEE Trans. Power Electron.*, vol. 35, no. 6, pp. 6501–6511, Jun. 2020.
- [45] L. Guo, S. Zhang, X. Li, Y. W. Li, C. Wang, and Y. Feng, "Stability analysis and damping enhancement based on frequency-dependent virtual impedance for DC microgrids," *IEEE J. Emerg. Sel. Topics Power Electron.*, vol. 5, no. 1, pp. 338–350, Mar. 2017.
- [46] S. Singh, A. R. Gautam, and D. Fulwani, "Constant power loads and their effects in DC distributed power systems: A review," *Renew. Sustain. Energy Rev.*, vol. 72, pp. 407–421, May 2017.
- [47] J. Lunze, *Regelungstechnik 2: Mehrgrößensysteme, Digitale Regelung: Mit 59 Beispielen, 105 Übungsaufgaben sowie einer Einführung in das Programmsystem MATLAB* (Lehrbuch), 9th ed. Berlin, Germany: Springer-Vieweg, 2016.
- [48] W. Inam, J. A. Belk, K. Turitsyn, and D. J. Perreault, "Stability, control, and power flow in ad hoc DC microgrids," in *Proc. IEEE 17th Workshop Control Modeling Power Electron. (COMPEL)*, Trondheim, Norway, Jun. 2016, pp. 1–8.
- [49] M. Amin and M. Molinas, "A gray-box method for stability and controller parameter estimation in HVDC-connected wind farms based on nonparametric impedance," *IEEE Trans. Ind. Electron.*, vol. 66, no. 3, pp. 1872–1882, Mar. 2019.
- [50] Y. Liu, A. Raza, K. Rouzbehi, B. Li, D. Xu, and B. W. Williams, "Dynamic resonance analysis and oscillation damping of multiterminal DC grids," *IEEE Access*, vol. 5, pp. 16974–16984, 2017.
- [51] M. Pulcherio, M. S. Illindala, J. Choi, and R. K. Yedavalli, "Robust microgrid clustering in a distribution system with inverter-based DERs," *IEEE Trans. Ind. Appl.*, vol. 54, no. 5, pp. 5152–5162, Sep. 2018.
- [52] N. Devarakonda and R. K. Yedavalli, "Determination of most desirable nominal closed-loop state space system via qualitative ecological principles," *J. Dyn. Syst., Meas., Control*, vol. 138, no. 2, Feb. 2016, Art. no. 021001.
- [53] T. Gönen, *Electric Power Distribution Engineering*, 3rd ed. Boca Raton, FL, USA: Taylor & Francis, 2014.
- [54] ME SOLshare, "SOLgrids in Bangladesh," Dhaka, Bangladesh, Tech. Rep. 2021-08, 2021.



Hannes Kirchhoff received the M.Sc. degree in renewable energy systems from TU Berlin, Germany, in 2013, where he is currently pursuing the Ph.D. degree with the Chair of Sustainable Electric Networks and Sources of Energy (SENSE).

He was a Technical Consultant with MicroEnergy International GmbH, Berlin, where he was involved in several projects in Asia and Africa undertaking technology, supplier, and value chain assessments. He is a Cofounder and the Chief Technology Officer of ME SOLshare, Singapore, and Dhaka, Bangladesh, where he is responsible for the development and deployment of innovative energy access solutions using direct current microgrid and mobile storage technologies.



Kai Strunz received the Dr.-Ing. degree (*summa cum laude*) from Saarland University, Saarbrücken, Germany, in 2001. He was with Brunel University in London from 1995 to 1997. From 1997 to 2002, he was with the Division Recherche et Développement of Electricité de France in Paris. From 2002 to 2007, he was Assistant Professor of electrical engineering with the University of Washington, Seattle, USA. Since 2007, he has been a Professor for Sustainable Electric Networks and Sources of Energy with TU Berlin in Germany. He has been a Guest Professor of the Chinese Academy of Sciences, Beijing, since 2017.

Dr. Strunz was the Chairman of the Conference IEEE Power and Energy Society (PES) Innovative Smart Grid Technologies Europe in 2012. He is the Chair of the IEEE PES Subcommittee "Distributed Energy Resources" and the Co-Chair of the IEEE Working Group "Dynamic Performance and Modeling of HVDC Systems and Power Electronics for Transmission Systems". He received the IEEE PES Prize Paper Award in 2015, the IEEE JOURNAL OF EMERGING AND SELECTED TOPICS IN POWER ELECTRONICS First Prize Paper Award 2015, and the 2020 best paper award in the field of electric machines and drives by IEEE TRANSACTIONS ON ENERGY CONVERSION. On behalf of the Intergovernmental Panel on Climate Change (IPCC), he acted as the Review Editor for the Special Report on Renewable Energy Sources and Climate Change Mitigation.